

North Pacific Influences on Long Island Sound Temperature Variability

JUSTIN A. SCHULTE AND NICKITAS GEORGAS

Davidson Laboratory, Stevens Institute of Technology, Hoboken, New Jersey

VINCENT SABA

NOAA/National Marine Fisheries Service, Northeast Fisheries Science Center, Geophysical Fluid Dynamics Laboratory, Princeton University, Princeton, New Jersey

PENELOPE HOWELL

Marine Fisheries Division, Connecticut Department of Energy and Environmental Protection, Old Lyme, Connecticut

(Manuscript received 3 March 2017, in final form 15 October 2017)

ABSTRACT

Climate indicators related to Long Island Sound (LIS) water and air temperature variability were investigated. The Pacific decadal oscillation (PDO) and east Pacific/North Pacific (EP/NP) patterns are found to be strongly correlated with LIS air temperature anomalies during most seasons, especially during the winter. Additionally, the winter EP/NP index is strongly correlated with subsequent spring and summer LIS water temperature anomalies, potentially rendering the EP/NP index useful in extended LIS water temperature outlooks. Such lagged relationships are found to be related largely to the decorrelation time scale of seasonal water temperature anomalies. The atmospheric circulation pattern associated with anomalous LIS water temperature conditions is consistent with atmospheric Rossby wave trains emanating from the western equatorial Pacific. The EP/NP index has a characteristic time scale of approximately 5 to 10 years and such fluctuations are termed the quasi-decadal mode, the mode identified as varying coherently with LIS air and water temperature anomalies. Apparent PDO and EP/NP regime shifts in 1997 are found to coincide with a LIS water temperature regime shift. This result suggests that not all LIS warming experienced during recent decades is solely due to anthropogenic causes but rather is to some extent a result of natural variability. The results from this study provide a useful framework for both seasonal and decadal prediction of LIS water temperature variability.

1. Introduction

It has been identified that modes of climate variability impact coastal water temperature variability. The impact of North Pacific sea surface temperature (SST) patterns such as the Pacific decadal oscillation (PDO; Mantua et al. 1997) and North Pacific Gyre Oscillation (NPGO; Di Lorenzo et al. 2008) on coastal water temperature variability across the U.S. West Coast is well established (Cloern et al. 2010). However, the influence of the PDO on eastern U.S. coastal waters is less clear because of uncertainty in how the PDO, a Pacific Ocean SST pattern, can influence atmospheric circulation patterns (Newman et al. 2016) that would act as an atmospheric bridge connecting PDO variability to water

temperature variability across remote regions. Recent work by Pershing et al. (2015) showed that rapid warming in the Gulf of Maine over the past decade was related to the Atlantic multidecadal oscillation (AMO; Kerr 2000), PDO, and Gulf Stream position fluctuations (Taylor 1995). Although Pershing et al. (2015) related changes in Gulf of Maine water temperature to the PDO, it is unknown how the PDO influences water temperature in other regions across the U.S. Northeast. In particular, the Long Island Sound (LIS) estuary is semienclosed by land and relatively shallow and therefore LIS water temperature may be less influenced by changes in the Gulf Stream position than Gulf of Maine water temperature. Thus, large-scale climate patterns important to Gulf of Maine water temperature variability may not be important to LIS water temperature variability. An additional study is therefore needed to

Corresponding author: Justin A. Schulte, jschulte@stevens.edu

DOI: 10.1175/JCLI-D-17-0135.1

© 2018 American Meteorological Society. For information regarding reuse of this content and general copyright information, consult the [AMS Copyright Policy](http://www.ametsoc.org/PUBSReuseLicenses) (www.ametsoc.org/PUBSReuseLicenses).

identify the large-scale climate patterns that influence LIS water temperature variability and to quantify the strength of such influences.

It is well documented that the mean global temperature has been rising but the warming is not spatially uniform. The rapid warming in the Gulf of Maine over the past decade exemplifies the role of climate modes such as the AMO and PDO in modulating regional temperature trends. Anomalous tropical forcing of the atmosphere consistent with a negative PDO has been shown to be related to hiatuses in global mean temperature trends (Trenberth et al. 2014). The impacts of these climate modes on temperature variability underscore the need to adopt seasonal temperature outlooks that incorporate the current behaviors of prominent climate oscillation patterns.

Other important North Pacific teleconnection patterns include the east Pacific/North Pacific (EP/NP) pattern, which has been shown to be strongly related to air temperature across the United States. As shown by Schulte and Lee (2017), U.S. air temperature relationships with the EP/NP index have been increasing since the 1950s. Such nonstationary relationships underscore the need to evaluate the impacts of climate modes on LIS water temperature in a nonstationary framework.

There also exists other well-known prominent modes of climate variability such as the North Atlantic Oscillation (NAO; Hurrell 1995), Arctic Oscillation (AO; Thompson and Wallace 1998), NPGO (Di Lorenzo et al. 2008), and El Niño–Southern Oscillation (ENSO). Schulte and Lee (2017) showed that the AO is not as well correlated with U.S. Northeast air temperature as the EP/NP index and Schulte et al. (2016) found no relationship between ENSO and air temperature across the mid-Atlantic region of the United States. These studies suggest that the AO and ENSO may not be important temperature indicators for the U.S. Northeast and the LIS.

Here we examined the hypothesis that LIS air and water temperature variability is influenced by North Pacific climate phenomena. In particular, we focus on the EP/NP pattern's impact on LIS water temperature variability because of its previously identified dominant influence on U.S. Northeast air temperature variability (Schulte and Lee 2017).

2. Data

Monthly-averaged water temperature data from 1979 to 2013 were obtained from a 34-yr hindcast generated from the New York Harbor Observing and Prediction System (NYHOPS; Georgas et al. 2016, and links therein). The model's ability to reproduce historical observed water temperature data was evaluated by Georgas et al. (2016),

who showed that the NYHOPS model can skillfully reproduce historical water temperature data provided by the Connecticut Department of Energy and Environmental Protection and New York City Department of Environmental Protection. As shown by Georgas et al. (2016), the root-mean-square error calculated between NYHOPS simulated and observed water temperature is 1.0°C, and a strong linear relationship between the simulated and observed water temperature exists. The reason for using the NYHOPS water temperature data is that observed data are sparse both spatially and temporally. The temporal sparseness of the observed data would preclude the use of wavelet analysis that requires continuous time series and the establishment of robust statistical climate mode–water temperature relationships that requires large sample sizes.

The model's horizontal resolution varies across the NYHOPS domain, ranging from 2.5 km to 250 m in the LIS region and its rivers. The model consists of 11 vertical levels based on a sigma coordinate system. In this study, the temperature data at vertical level 1 will be referred to as surface water temperature and the data at vertical level 11 will be referred to as bottom water temperature. LIS bottom and surface water temperature were created by spatially averaging the bottom and surface water data in the gray-shaded region shown in Fig. 1a. The seasonal cycles were removed from the time series by subtracting the 1979–2013 mean monthly value for each month from the corresponding monthly values for each month.

Data for the PDO index from 1979 to 2013 were obtained from the University of Washington (available at <http://research.jisao.washington.edu/pdo/PDO.latest>). The PDO index is defined as the leading empirical orthogonal function (EOF) of monthly North Pacific SSTs poleward of 20°N. The NPGO index (available at <http://www.o3d.org/npgo/>) was also used to quantify the impacts of North Pacific SSTs on the LIS. The NPGO represents the second leading mode of sea surface height variability in the North Pacific and closely follows the second leading mode of SST variability sometimes called the North Pacific mode (Di Lorenzo et al. 2008; Hartmann 2015). Data for the EP/NP index were obtained from the Climate Prediction Center (CPC) and the index was calculated from a rotated principal component analysis of 500-hPa geopotential height anomalies. Indices for the Pacific–North American teleconnection pattern (PNA; Wallace and Gutzler 1981) and the west Pacific (WP; Barnston and Livezey 1987) were obtained from the CPC and were calculated from a rotated principal component analysis of 500-hPa geopotential height anomalies.

For the PDO and EP/NP indices, extended time series spanning, respectively, the periods 1900–2013 and 1950

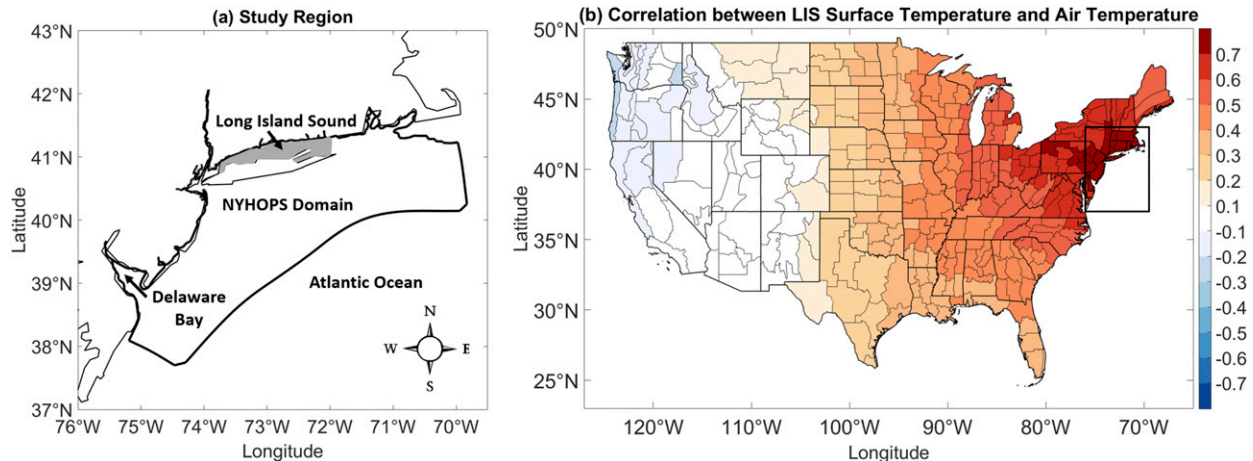


FIG. 1. (a) The NYHOPS domain (thick black contoured region) and the Long Island Sound (gray shading). (b) Correlation between monthly LIS monthly surface water temperature anomalies and U.S. climate divisional mean monthly temperature anomalies. Only climate divisions (thin black lines) for which correlation coefficients are statistically significant at the 5% significance level are shaded.

to 2013 were also used to maximize the usefulness of the wavelet spectral analysis. For all other analyses and climate indices, the period of record was restricted to 1979 to 2013 to overlap with the time interval of available LIS data. Missing EP/NP December data were filled based on the correlation between the EP/NP index and 300-hPa streamfunction anomalies over Alaska (Schulte and Lee 2017). The December data are missing because apparently the December EP/NP pattern does not exist. The nonexistence of the EP/NP pattern could be an artifact of the principal component analysis used to construct the index because U.S. temperature variability in December is related to a pattern very similar to the EP/NP pattern (Schulte and Lee 2017). The 64 missing December values were filled by first correlating the EP/NP index with 300-hPa streamfunction anomalies using only data for January and February, where the correlation calculation was restricted to January and February because the EP/NP index is most strongly correlated with 300-hPa streamfunction anomalies during those months. We then extracted the monthly 300-hPa streamfunction anomaly time series at the grid point for which the correlation coefficient is the largest. The maximum correlation coefficient was found to be -0.75 , which corresponds to a grid point located over Alaska. The monthly February and January 300-hPa streamfunction anomalies were then linearly regressed with the February and January EP/NP indices and the resulting linear relationship was used to fill the missing EP/NP December values based on the available December 300-hPa streamfunction anomalies at the grid point.

Results using the North Pacific climate indices were compared to those obtained using indices describing the

AMO, NAO, and the Gulf Stream position. The NAO and AMO indices from 1979 to 2013 were obtained from the CPC. The Gulf Stream Index (GSI; available at <http://www.pml-gulfstream.org.uk/>) describes the position of the north wall of Gulf Stream and is calculated from a principal component analysis of the position of the north wall of the Gulf Stream (Taylor 1995).

The European Centre for Medium-Range Forecasts (ECMWF) interim reanalysis (ERA-Interim) SST, 300-hPa streamfunction, and 2-m air temperature reanalysis data were also used. The grid spacing for 2-m air temperature and 300-hPa streamfunction was 0.125° latitude and 0.125° longitude and for SST was 0.75° latitude and 0.75° longitude for SST.

Observed U.S. climate divisional mean monthly temperature data (Guttman and Quayle 1996) were used to create a monthly LIS regional air temperature time series (referred to hereafter as the LIS air temperature time series for brevity). The time series was first created by correlating LIS surface temperature anomalies with U.S. climate divisional mean monthly temperature anomalies (Fig. 1b), where the air temperature anomalies were computed by subtracting the 1979 to 2013 monthly means for each month from the monthly values for the same month. For this correlation analysis, trends were not removed from the monthly air and water temperature data because trends in water temperature should be physically related to trends in air temperature. The next step in creating a LIS air temperature time series involved the computation of an area-weighted average monthly air temperature anomaly time series using all air temperature anomaly time series that are strongly correlated ($r > 0.70$) with LIS surface water temperature

anomalies. The weights were determined based on the area of the climate division associated with each climate divisional air temperature anomaly time series. The climate divisions used in the calculation are shown in dark red in Fig. 1b. Three monthly LIS air temperature time series were constructed, one for the 1979 to 2013 time period, a second one for the 1950 to 2013 period, and a third one for the 1900–2013 period. The anomalies for the three time series were based on 1979–2013 monthly means. The 1900–2013 and 1950–2013 time series were only used for the wavelet analysis.

There are two benefits to using these LIS air temperature time series for the present analysis. The first benefit is that two of the LIS air temperature time series are longer than the LIS water temperature time series. The two relatively long LIS air temperature time series makes them useful for identifying low-frequency relationships between the EP/NP index and LIS air temperature anomalies that then can be used to extrapolate historical climate index relationships with LIS water temperature. A second benefit is that the LIS air temperature time series is defined on a larger spatial scale than the LIS water temperature time series, reducing the possibility that climate index relationships with air temperature are the result of feedbacks of LIS water temperature onto air temperature.

3. Methods

a. Correlation analysis

Lagged relationships between seasonally averaged water temperature and seasonally averaged climate indices were quantified using a lagged correlation analysis. In particular, we adopted the Pearson correlation coefficient for the computation of statistical relationships. The statistical significance of the correlation coefficients was assessed using a Student's t distribution for a transformation of the correlation. Correlation coefficients were computed between seasonal means, respectively, as fall [September–November (SON)], winter [December–February (DJF)], spring [March–May (MAM)], and summer [June–August (JJA)]. Other seasons were defined as a period of three consecutive months. For example, August through October (ASO) and April through June (AMJ) were considered seasons. Two seasons were said to be different if at least one month composing one season does not belong to the other. Annual means were calculated based on the calendar year.

The time series were linearly detrended to avoid spuriously large correlation coefficients between otherwise unrelated time series. The time series were detrended by first computing a least squares fit of a

straight line to the data and then subsequently subtracting the resulting function from the data. Seasonal means were first computed then the seasonal time series were detrended separately, one least squares fit of a straight line for each season. The reason for detrending the seasonal time series separately is that the magnitude of the trends vary. The seasonal means were also detrended individually before the computation of the correlation coefficients.

Throughout the paper detrended results are shown. However, correlation analyses were conducted using both detrended and raw temperature data to check the sensitivity of results to the removal of trends, and cases are highlighted where detrending resulted in substantial differences in findings. The reason for checking the sensitivity of results is that detrending the temperature data does not necessarily imply that the trend removed is related exclusively to anthropogenic forcing.

b. Wavelet analysis

Nonstationary characteristics of the monthly climate time series and nonstationary relationships between monthly climate and temperature time series were quantified using wavelet analysis. The wavelet transform of a time series X is given by

$$W_n^X(s) = \sqrt{\frac{2\delta t}{s}} \sum_{n'=0}^{N-1} x_{n'} \psi^* \left[\frac{(n' - n)\delta t}{s} \right], \quad (1)$$

where ψ is the Morlet wavelet given by

$$\psi(\eta) = \pi^{-1/4} e^{i\omega_0 \eta} e^{-\frac{1}{2}\eta^2}, \quad (2)$$

$\omega_0 = 6$ is the dimensionless frequency, t is time, s is the wavelet scale, δt is a time step determined from the data (1 month here), N is the length of the time series, and $\eta = st$ (Torrence and Compo 1998). The Morlet wavelet was adopted for this study because it balances frequency localization and time localization (Grinsted et al. 2004). The asterisk in Eq. (1) denotes the complex conjugate. The wavelet transform was computed at a discrete set of scales ($s_j; j = 0, 1, \dots, J$), with

$$s_j = s_0 2^{j\delta}, \quad (3)$$

$$J = \delta^{-1} \log_2 \left(\frac{N\delta t}{s_0} \right), \quad (4)$$

and $\delta = 0.5$.

To quantify the relationships between climate modes and water temperature as a function of frequency and time, a wavelet coherence analysis was conducted. Following Grinsted et al. (2004), the (local) wavelet

squared coherence between two time series X and Y is given by

$$R_n^2(s_j) = \frac{|S[s_j^{-1} W_n^{XY}(s_j)]|^2}{S[s_j^{-1} |W_n^X(s_j)|^2] S[s_j^{-1} |W_n^Y(s_j)|^2]}, \quad (5)$$

where $W_n^{XY}(s_j)$ is the cross-wavelet transform at time index n and scale s_j . The cross-wavelet power, $W_n^{XY}(s_j)$, is defined as the product of the wavelet transform of X and the complex conjugate of the wavelet transform of Y . In Eq. (5), S is a smoothing operator defined by $S[W_n(s_j)] = S_{\text{scale}}\{S_{\text{time}}[W_n(s_j)]\}$, where S_{time} represents smoothing in time and S_{scale} is smoothing along the wavelet scale axis. Using Monte Carlo methods, the statistical significance of wavelet squared coherence was found by generating a large number of surrogate red noise time series pairs with the same lag-1 autocorrelation coefficients as the input time series and computing the wavelet coherence between each pair (Grinsted et al. 2004).

Spurious results in wavelet analysis can result from the simultaneous testing of multiple hypotheses (Maraun and Kurths 2004; Maraun et al. 2007; Schulte et al. 2015; Schulte 2016). For this reason the cumulative areawise test developed by Schulte (2016) was applied to control the number of false positive results. The test is preferred to other existing areawise (Maraun et al. 2007) and geometric (Schulte et al. 2015) tests because the cumulative areawise test has greater statistical power and circumvents the problem of having to choose two significance levels for a single statistical test (Schulte 2016). The test makes use of how contiguous regions of pointwise significance (significance patches) arise from the application of the pointwise test because of the correlation among adjacent wavelet coefficients. To apply the test, normalized areas of pointwise significance patches were computed over a discrete set of pointwise significance levels, where the normalized area is defined as the patch area divided by the square of its centroid's scale coordinate and is used to compare the areas of patches at different scales simultaneously (Schulte et al. 2015). In this study, the normalized areas were computed for pointwise significance levels $\alpha = 0.02$ to $\alpha = 0.18$, with the spacing between adjacent pointwise significance levels being 0.02. The reason for choosing this discretization of the pointwise significance levels was that this method produced good statistical power (Schulte 2016).

To measure relationships at particular frequencies, the *global coherence* (Schulte et al. 2016) between two time series was computed. The global coherence spectrum is a time-averaged representation of local wavelet squared coherence defined in Eq. (5). The time-averaged wavelet squared coherence is given by

$$G_C(s_j) = \frac{|W^{XY}(s_j)|^2}{\left[\sum_{n=1}^N |W_n^X(s_j)|^2 \right] \left[\sum_{n=1}^N |W_n^Y(s_j)|^2 \right]}, \quad (6)$$

where

$$W^{XY}(s_j) = \sum_{n=1}^N W_n^X(s_j) W_n^{Y*}(s_j) \quad (7)$$

(Elsayed 2006; Schulte et al. 2016). Equation (6) measures the coherence between two time series in the entire study period at a scale s_j . The statistical pointwise significance of $G_C(s_j)$ was computed using Monte Carlo methods in a similar manner as for local wavelet coherence. In this study the global coherence spectra are used to better identify the time scales at which coherence is the largest.

A modified version of the cumulative areawise test was also applied to the global coherence spectra to reduce the number of false positive results. The test assessed the statistical significance of peaks against a red-noise background based on arc length instead of area as in the full coherence spectrum (see the appendix); referred to hereafter as the *arcwise test*. More specifically, the arc lengths of the portion of the peaks that were above the critical level of the test corresponding to the pointwise significance level α were computed. The arc length of the peaks was computed for pointwise significance levels $\alpha = 0.02$ to $\alpha = 0.18$, with the spacing between adjacent pointwise significance levels being 0.02. The reason for choosing this discretization was to be consistent with the cumulative areawise test. A test statistic called the *cumulative arc length* was then defined as the cumulative sum of the arc lengths across all pointwise significance levels. Here, we used normalized arc lengths, which were calculated using the logarithm of wavelet scales. Normalization is necessary because peaks widen with increasing scale because the decorrelation length of the Morlet wavelet increases with scale (Maraun et al. 2007). The null distribution was obtained by generating surrogate red noise time series in the same manner as the cumulative areawise test and computing the null distribution of arc lengths. The cumulative arc length test statistic was then compared to the null distribution of cumulative arc lengths under the null hypothesis of red noise.

4. Results

a. LIS time series

The most salient features of the nondetrended time series for LIS air temperature, surface water temperature,

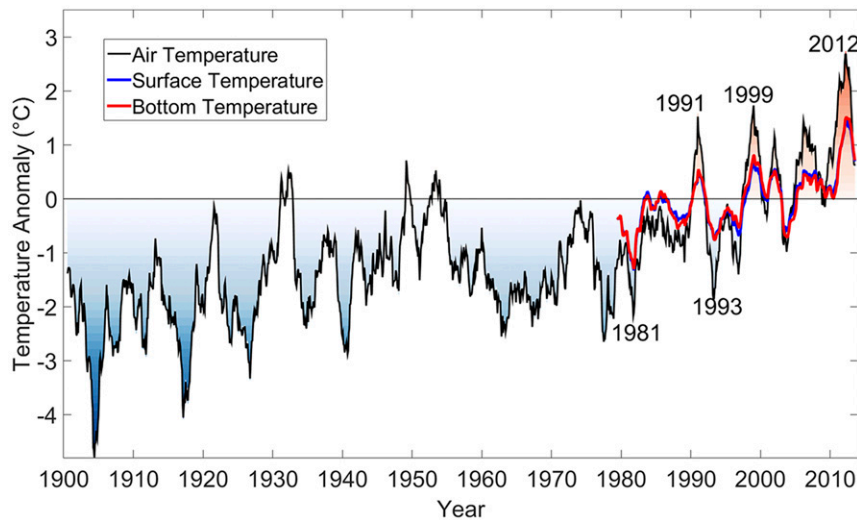


FIG. 2. 12-month running means of (a) LIS air, (b) surface water, and (c) bottom water temperature anomalies.

and bottom temperature anomalies are the prominent anomalous warm events in 1999 and 2012 (Fig. 2). Other notable events are the 1991 warm period and the cold periods in 1981, 1993, and 2011. An inspection of Fig. 2 reveals that the LIS air temperature time series appears to have fluctuated coherently with the time series for both surface ($r = 0.93$; $p < 0.001$) and bottom temperature ($r = 0.92$; $p < 0.001$) time series. The result suggests that atmospheric processes associated with changes in air temperature are likely the primary mechanisms governing LIS water temperature variability. Another notable feature of Fig. 2 is that for all three time series colder-than-normal conditions are more frequent earlier in the record and warmer-than-normal conditions are more frequent later in the record.

b. PDO and EP/NP indices

The PDO index from 1900 to 2013 together with its wavelet power spectrum shows low-frequency variability of the raw monthly PDO index (Fig. 3a). A noteworthy feature is the persistent and strongly negative PDO index extending from 2010 to 2012. The lack of statistically significant wavelet power for the raw monthly PDO index (Fig. 3b) suggests that the PDO index has no intrinsic time scale so that fluctuations in the PDO index may be stochastic. The higher wavelet power at low frequencies together with the nonexistence of statistical significance suggests that the PDO is consistent with a red-noise process with a long decorrelation time scale. As noted by Chan and Zhou (2005), the strongest PDO signal is in the 16–32-yr period band but the results from the present analysis suggest that the wavelet power in the 16–32-yr period band is indistinguishable from a

red-noise background. Although Lara et al. (2016) found statistically significant wavelet power at a period of 12 months, our results suggest that PDO fluctuations at that the time scale are also stochastic. The results from the present wavelet analysis are consistent with the idea that the PDO is an integrated response to ENSO and atmospheric forcing and not an intrinsic oscillatory pattern in the climate system.

As shown in Fig. 4, the monthly EP/NP index is noisy but prominent features are still identifiable from an inspection of the raw time series (Fig. 4a). For example, 2011 and 2012 consist of near-record negative EP/NP indices and all 12 calendar months in 2011 are identified with negative EP/NP indices (Fig. 5). The positive LIS water temperature anomalies during those years are unprecedented compared to water temperature anomalies at other times in the 34-yr hindcast, suggesting a possible link between the EP/NP pattern and the variability of anomalies for LIS air and water temperature.

The wavelet power spectrum of the EP/NP index (Fig. 4b) shows enhanced 5- to 10-yr variability that exceeds a red-noise background. The statistically significant wavelet power in the 5- to 10-yr period band (region bounded by dotted lines in Fig. 4b) extends throughout the record length but the statistical significance declines at the edges of the record. It is unclear, however, if the reduction in statistical significance is physical or due to edge effects inherent in wavelet analysis that are not negligible in the cone of influence (Torrence and Compo 1998) depicted by the light shading in Fig. 4b.

The EP/NP time series was smoothed based on the results of the wavelet analysis to highlight the quasi-decadal

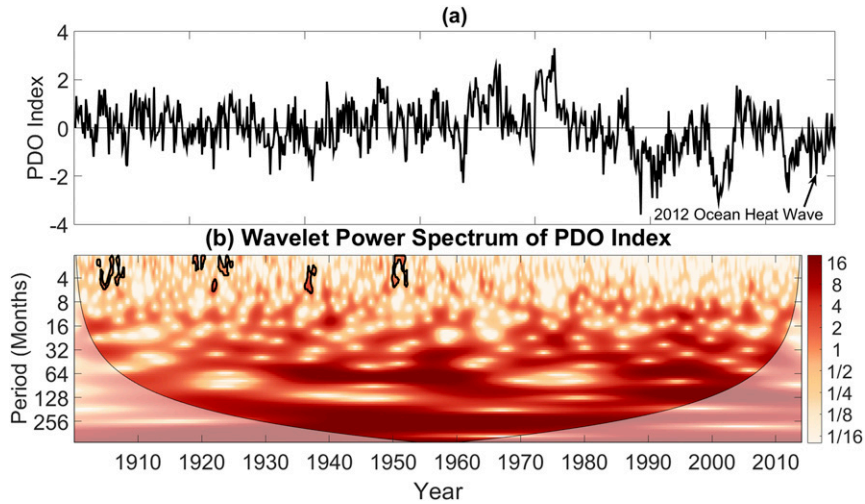


FIG. 3. (a) Raw monthly PDO index from 1900 to 2013 and (b) its corresponding wavelet power spectrum. Contours enclose regions of 5% cumulative areawise significance. Light shading represents the cone of influence, the region in which edge effects are not negligible.

variability. A filtered time series was calculated by setting all wavelet coefficients to zero except those in the period band indicated by the dotted lines in Fig. 4b and then taking the inverse wavelet transform of the resulting set of wavelet coefficients. The resulting time series from the procedure, hereafter referred to as the quasi-decadal mode, has an amplitude that changes with time. The quasi-decadal mode around the 1900, 1999, and 2012 warm periods (Fig. 2) is in a negative phase. On the other hand, the relatively cool period in the mid-1990s coincides with a positive phase of the quasi-decadal mode. The quasi-decadal mode does not switch sign in

2008 and so neither negative nor positive EP/NP indices are preferred (thin black curve) around that time.

c. Correlation with climatic fields

As shown in Fig. 1b, monthly LIS surface water temperature anomalies are positively correlated with monthly air temperature anomalies across the eastern two-thirds of the U.S. and negatively related to air temperature anomalies across the U.S. west coast. The negative correlation coefficients located across the U.S. west coast suggest that LIS water temperature variability is related to a large-scale climate pattern.

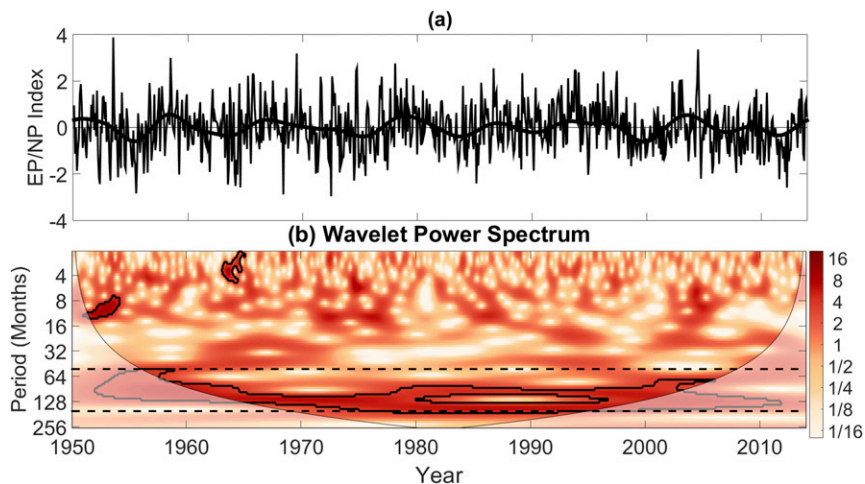


FIG. 4. (a) Raw monthly EP/NP index and the quasi-decadal mode (thick black curve) of the EP/NP index. (b) As in Fig. 3b, but for the raw monthly EP/NP index. Dotted lines bound the period band in which statistically significant wavelet power was identified at quasi-decadal time scales.

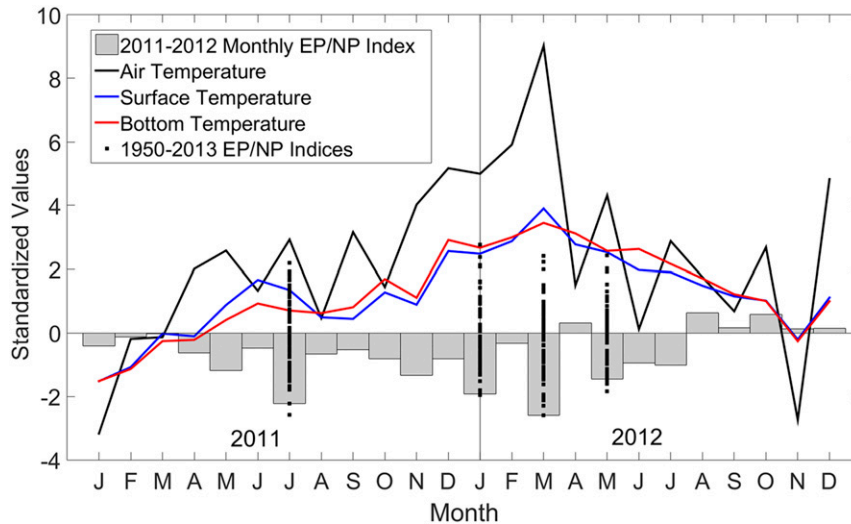


FIG. 5. Raw monthly time series for the EP/NP index and standardized monthly anomaly time series for air temperature, surface temperature, and bottom temperature from January 2011 to December 2012. Black squares represent the raw monthly EP/NP indices for the month indicated on the horizontal axis for the period 1950 to 2013.

To show LIS water temperature anomalies are related to a large-scale climate pattern, we correlated monthly LIS surface water temperature anomalies with monthly SST anomalies (Fig. 6a). The results from the analysis show that LIS water temperature anomalies are negatively correlated with SST anomalies along the U.S. West Coast and positively correlated with SST anomalies across the central North Pacific Ocean. A comparison of Fig 6a with Figs. 6b and 6c shows that the correlation pattern resembles that obtained by correlating the indices for the PDO and EP/NP with SST anomalies. All three time series are correlated with SST anomalies across the western tropical Pacific, a region where tropical convection is especially effective at exciting Rossby waves (Simmons et al. 1983; Palmer and Mansfield 1984) because SSTs there are among the warmest in the world (Palmer 2014).

Some differences between the correlation patterns are evident. For example, the PDO index is correlated with SST anomalies across the eastern equatorial Pacific, whereas LIS surface water temperature anomalies are not. It thus appears that LIS water temperature variability is related to Pacific SST variability unrelated to canonical ENSO. Evidence for the lack of relationship with ENSO was supported by correlating common monthly indices describing ENSO, such as the Niño-1.2 and Niño-3.4 indices, with the monthly temperature anomaly time series for LIS air and water temperature. The analysis identified no statistically significant relationships with any of the ENSO metrics, supporting the idea that ENSO is not directly a climate pattern influencing LIS temperature anomalies.

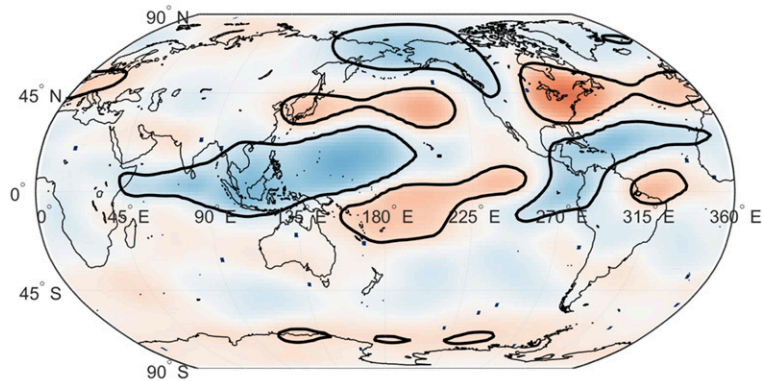
The results from the correlation analysis between LIS water temperature anomalies and 300-hPa streamfunction anomalies suggest that LIS water temperature anomalies are associated with Rossby wave trains emanating from the western equatorial Pacific (Fig. 7a). The correlation pattern also shows that monthly LIS surface water temperature anomalies are negatively correlated with 300-hPa streamfunction anomalies over Alaska and the western equatorial Pacific. The correlation pattern is also such monthly LIS water temperature anomalies are positively correlated with 300-hPa streamfunction anomalies over the central equatorial Pacific, North Pacific Ocean, and U.S. Northeast. A comparison of the correlation pattern shown in Fig. 7a with those associated with the PDO and EP/NP indices (Figs. 7b,c) reveals similarities in the 300-hPa streamfunction patterns. In particular, both the monthly EP/NP index and monthly LIS surface temperature anomalies are correlated with 300-hPa streamfunction anomalies across the western Pacific and over Alaska, and thus positive monthly EP/NP indices and negative monthly LIS surface water temperature anomalies are associated with a jet stream ridge over Alaska. The PDO index is not correlated with 300-hPa streamfunction anomalies over Alaska but is associated with negative 300-hPa streamfunction anomalies across the majority of the contiguous United States.

d. Correlation with climate indices

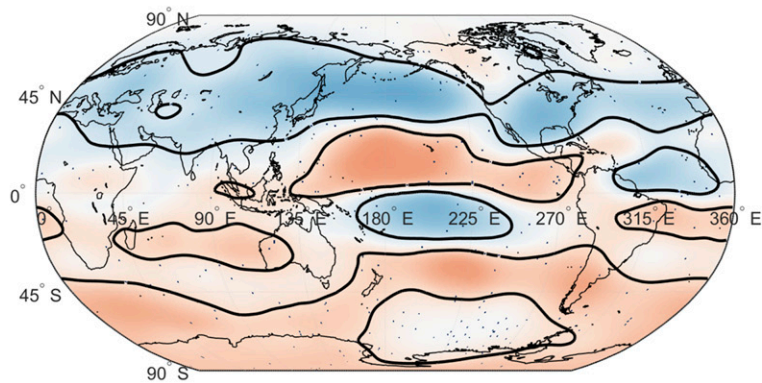
The similarity between the correlation patterns shown in Figs. 7a and 7c suggests that the EP/NP pattern is

Correlation between 300-hPa Streamfunction and Climate Indices

(a) LIS Surface Temperature



(b) PDO Index



(c) EP/NP Index

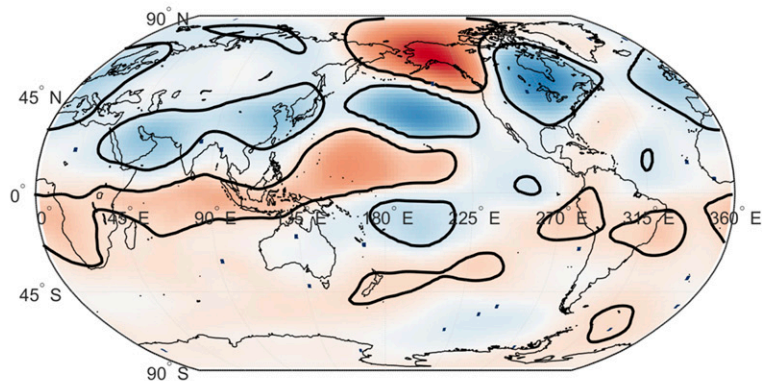


FIG. 6. (a) Correlation between LIS surface water temperature anomalies and SST anomalies from 1979 to 2013. Contours enclose regions of 5% statistical significance. (b) As in (a), but for the PDO index. (c) As in (a), but for the EP/NP index.

Correlation between SST and Climate Indices

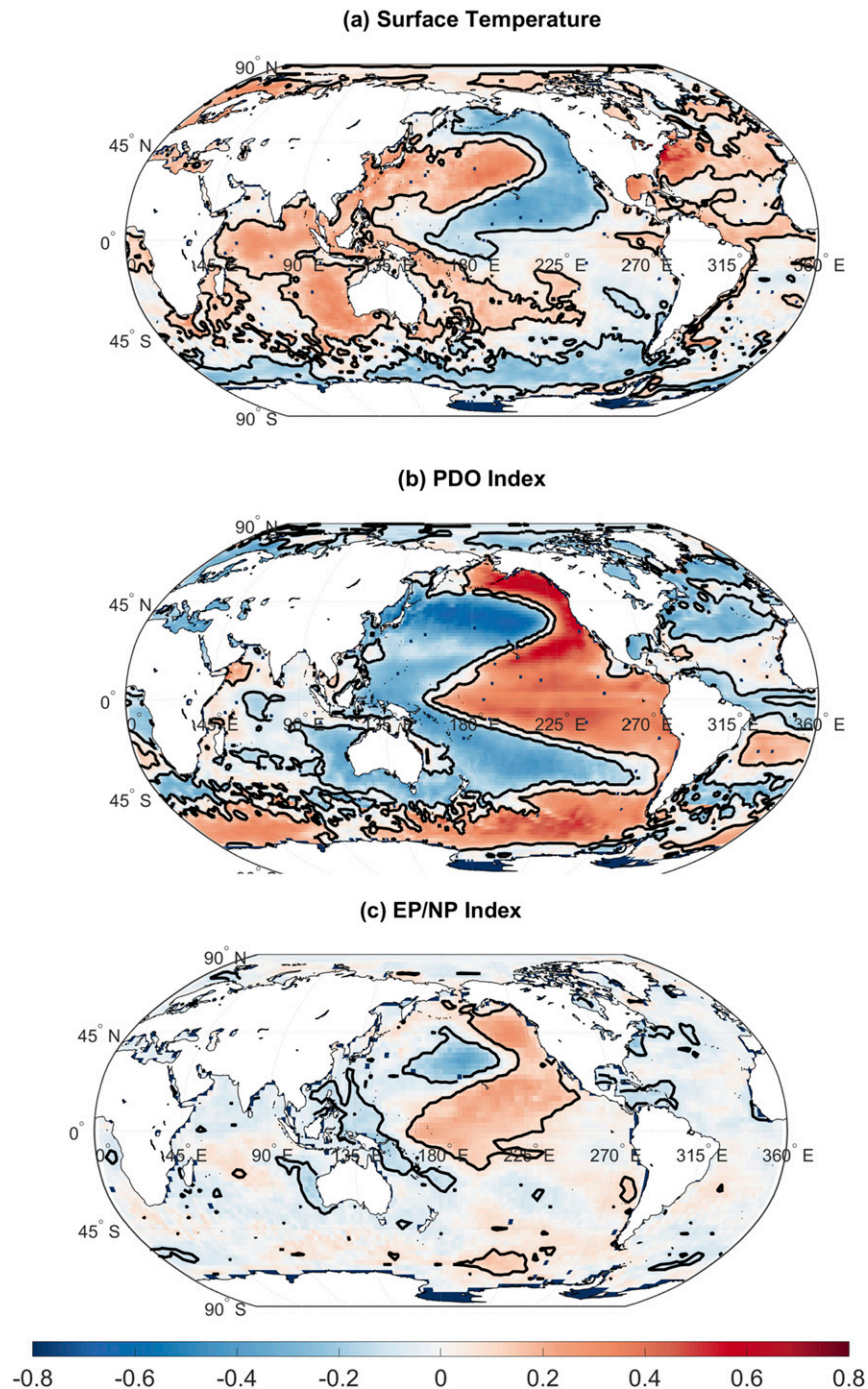


FIG. 7. (a) As in Fig. 6a, but for 300-hPa streamfunction anomalies. (b) As in Fig. 6b, but for 300-hPa streamfunction anomalies. (c) As in Fig. 6c, but for 300-hPa streamfunction anomalies.

related to LIS water temperature anomalies and therefore it is reasonable to correlate LIS water temperature anomalies with various large-sale climate indices to identify possible relationships with the associated climate

patterns. The results from the correlation analysis between seasonally averaged detrended LIS temperature anomalies and various seasonally averaged climate indices are shown in Table 1. The results show statistically

TABLE 1. Pearson correlation between various climate indices and detrended anomaly time series for LIS air, surface, and bottom temperature from 1979 to 2013 for winter, spring, summer, fall, and annual mean. Bold entries are statistically significant at the 5% level.

	DJF	MAM	JJA	SON	Annual
	Air temperature				
EP/NP	-0.65	-0.50	-0.31	-0.43	-0.46
NPGO	0.09	0.25	0.06	-0.02	0.18
WP	0.14	0.44	-0.30	0.30	0.13
PNA	0.12	-0.14	0.03	0.02	0.00
PDO	-0.35	-0.23	-0.07	-0.40	-0.26
NAO	0.29	-0.01	0.04	0.34	-0.17
GSI	0.01	-0.20	0.16	-0.16	0.06
AMO	0.13	0.07	0.28	0.13	0.21
	Surface temperature				
EP/NP	-0.57	-0.31	-0.31	-0.15	-0.39
NPGO	-0.03	0.40	0.35	-0.02	0.28
WP	0.21	0.30	-0.17	0.17	-0.02
PNA	0.18	-0.09	-0.08	0.00	0.02
PDO	-0.28	-0.35	-0.42	-0.29	-0.31
NAO	0.35	-0.05	-0.12	0.37	-0.08
GSI	0.05	-0.03	0.23	0.06	0.18
AMO	0.03	0.12	0.33	0.10	0.15
	Bottom temperature				
EP/NP	-0.56	-0.23	-0.14	-0.17	-0.35
NPGO	-0.06	0.39	0.28	-0.02	0.26
WP	0.21	0.27	-0.16	0.17	-0.05
PNA	0.18	-0.14	-0.19	-0.04	-0.03
PDO	-0.27	-0.36	-0.45	-0.31	-0.33
NAO	0.35	-0.08	-0.17	0.39	-0.07
GSI	0.04	0.00	0.33	0.06	0.21
AMO	0.00	0.12	0.19	0.10	0.11

significant relationships between winter (DJF) anomalies for water and air temperature and DJF indices for the EP/NP and PDO. The magnitude of the correlation coefficients calculated between the DJF EP/NP index and DJF anomalies for LIS air and water temperature anomalies exceeds 0.55. In comparison, the magnitude of the correlation coefficients corresponding to the DJF NAO and PDO analyses do not exceed 0.35. These results suggest that the DJF EP/NP pattern is the dominant pattern associated with DJF LIS water and air temperature variability. The results are consistent with how the EP/NP index is associated with changes in the eastern U.S. trough (Fig. 7c), where jet stream troughs are associated with cooler-than-normal surface conditions. The results do not support a dominant role played by other well-known large-scale climate phenomena.

The EP/NP pattern also emerges as the dominant climate mode in the spring, although the MAM WP index is also correlated with MAM LIS air temperature anomalies. The EP/NP–air temperature relationships for the JJA and SON seasons are weaker than those for the MAM season. The SON PDO index is moderately

correlated with SON air temperature ($r = -0.40$) but weakly correlated with SON LIS water temperature anomalies. The JJA PDO index is also moderately correlated ($r \approx -0.45$) with JJA anomalies for surface and bottom water temperature anomalies but the JJA PDO index is only weakly correlated with JJA LIS air temperature anomalies, suggesting a possible lag relationship between LIS air temperature and water temperature anomalies (section 4g).

The annually averaged PDO and EP/NP indices are most correlated with both mean annual LIS air and water temperature anomalies. Neither the annual mean NAO index nor the annual mean GSI is significantly correlated with annual mean air or water temperature anomalies despite the proximity of the LIS to the Atlantic Ocean. However, the DJF and SON NAO index is correlated with LIS water temperature anomalies for the DJF and SON seasons.

The DJF indices for the PDO, EP/NP, and NAO were correlated to both DJF surface and bottom water temperature anomalies across the NYHOPS domain to identify spatial patterns in the climate mode–water temperature relationships (Fig. 8). Both DJF surface and bottom winter water temperature anomalies are most strongly correlated with the DJF EP/NP index, with correlation coefficients approaching -0.7 near the mouth of the Hudson River and in regions surrounding the Delaware Bay. Correlation coefficients range from -0.7 to -0.6 in the LIS. For both DJF surface and bottom temperature anomalies, relationships are weaker with the DJF PDO index. Note that the DJF EP/NP index relationships with DJF bottom water temperature anomalies weaken away from the land. Physically, the gradient in the magnitude of the correlation coefficients can be interpreted as the result of water depth being shallow along the shelf where vertical mixing can readily communicate surface water temperature anomalies arising from atmospheric fluctuations to the bottom waters. In the open ocean, the local water depth is much deeper than the mixed-layer depth so only strong vertical mixing would communicate surface water temperature anomalies to the bottom waters.

The results from the correlation analysis between the DJF NAO and DJF water temperature anomalies (Figs. 8e,f) show that statistically significant relationships are mainly located across southwestern portions of the NYHOPS domain. The DJF GSI is only correlated with DJF water temperature anomalies around the eastern edge of the NYHOPS domain (Figs. 8g,h). These results suggest that wintertime water temperature variability in this region is dominated by atmospheric fluctuations associated with the EP/NP pattern.

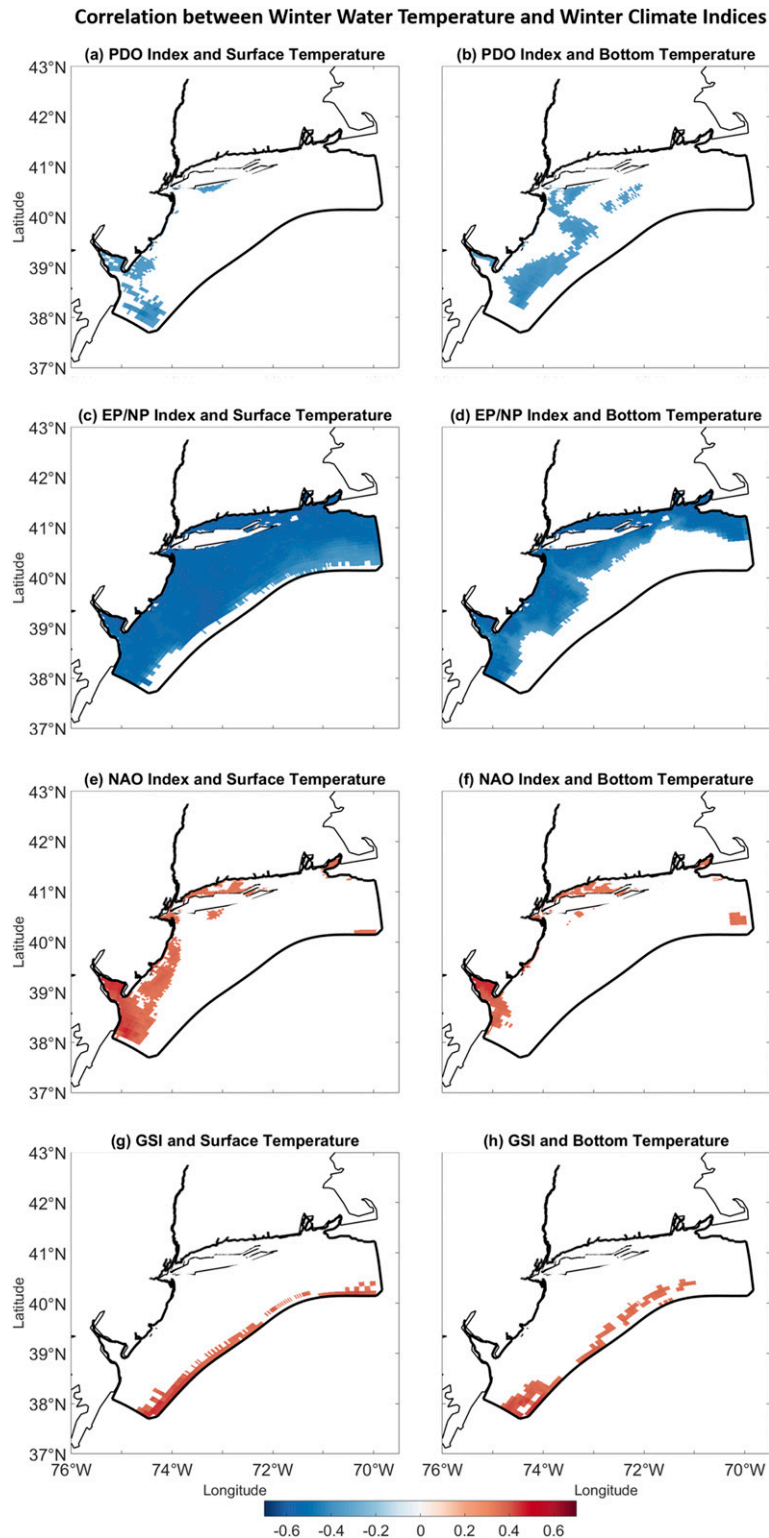


FIG. 8. Correlation between winter water and winter climate indices for the NYHOPS domain's surface and bottom water and winter indices for the (a),(b) PDO, (c),(d) EP/NP, (e), (f) NAO, and (g),(h) Gulf Stream position from 1979 to 2013. Only correlation coefficients statistically significant at the 5% level are displayed.

A similar analysis was conducted for the other seasons. The results from the summer correlation analysis show that the JJA PDO index is correlated with JJA surface and bottom water temperature anomalies across the NYHOPS domain (Fig. 9), the strongest relationships located in and around the LIS. Negative correlations between JJA LIS surface water temperature anomalies and the JJA EP/NP index are located around the LIS but few relationships are statistically significant.

Correlations between water temperature anomalies and the climate indices are generally weaker during the other seasons. The larger correlation coefficients found in the DJF analysis compared to the other seasons are consistent with how most teleconnection patterns are most pronounced during winter. However, unlike in winter, strong and statistically significant JJA NAO–water temperature (Figs. 9e,f) and JJA GSI–water temperature (Figs. 9g,h) relationships are located across portions of the NYHOPS domain. The statistically significant JJA GSI–water temperature relationships are confined to eastern portions of the NYHOPS domain (Figs. 9g,h). This result is consistent with how the eastern portion of the NYHOPS domain is located closer to the Gulf Stream than western portions of the study region.

The results from the correlation analyses presented in Table 1 and Figs. 8 and 9 are not sensitive to the removal of long-term temperature trends except for one notable exception. The AMO index is more correlated with LIS water temperature when the LIS water temperature time series contain the trends. For example, the annual mean LIS surface water temperature time series is strongly correlated with the annual mean AMO index ($r = -0.6$) when the LIS surface water temperature time series contains the long-term trend. The sensitivity of the results to the linear detrending could mean that part of the LIS water temperature trend is related to the low-frequency variability of the AMO. However, it is unclear how the AMO could influence LIS water temperature variability given that monthly air temperature fluctuations are so strongly related to monthly LIS water temperature fluctuations (Fig. 1b).

e. Cross-correlation analysis

Although robust relationships between seasonally averaged climate indices and seasonally averaged anomaly time series for air and water temperature were identified in section 4d, the analysis did not account for possible lag relationships. To account for possible lag relationships, we computed the cross-correlation between detrended seasonally averaged anomalies for LIS air and water temperature and seasonally averaged

climate indices. The analysis focused on the EP/NP pattern because of its strong and consistent relationships with LIS water temperature anomalies (Table 1).

The results of the cross-correlation analysis are presented in Fig. 10. The vertical axis of Fig. 10 refers to the lead time (in seasons) of the seasonally averaged EP/NP index so that distance from the horizontal axis is proportional to the lead time of the seasonally averaged EP/NP index. For example, the green square is centered in the shaded rectangle representing the correlation between the DJF EP/NP index and MAM detrended anomalies for LIS air or water temperature (because the y-axis value is three seasons after the EP/NP index). Similarly, the green circle is centered in the rectangle representing the correlation between the DJF EP/NP index and JJA detrended anomalies of LIS air and water temperature. The green diamond, as another example, is located within the rectangle representing the correlation between the DJF EP/NP index and SON detrended anomalies for LIS air and water temperature.

The results shown in Fig. 10 indicate that the seasonally averaged EP/NP index is most strongly related to seasonally averaged LIS air and water temperature anomalies in the winter. For LIS water temperature, the DJF EP/NP index is generally more strongly related to water temperature when the DJF EP/NP index leads by 1 to 3 seasons than when the DJF EP/NP index leads by 0 seasons. That is, Fig. 10 suggests that the DJF EP/NP index is a good predictor of what seasonally averaged LIS water temperature anomalies will be in the subsequent January–March (JFM), February–April (FMA), and MAM seasons. These lagged DJF EP/NP index relationships with LIS water temperature anomalies explain why the DJF EP/NP index relationship with DJF LIS air temperature anomalies is stronger than the DJF EP/NP index relationship with DJF LIS water temperature anomalies as shown in Table 1. Figure 10 also shows that the DJF EP/NP index is significantly correlated with JJA LIS water temperature anomalies (lag = 6 seasons).

A similar cross-correlation analysis was conducted but with the seasonally averaged PDO index (not shown). The results are generally similar because the PDO and EP/NP indices are correlated, especially during the fall (not shown). The seasonally averaged EP/NP index is generally more strongly cross-correlated with seasonally averaged LIS air and water temperature anomalies than the seasonally averaged PDO index. The lagged relationship between the DJF EP/NP index and JJA water temperature anomalies together with the correlation between the EP/NP and PDO indices also explains why the JJA PDO index is correlated with JJA LIS water temperature anomalies but not with JJA LIS air temperature anomalies (Table 1).

Correlation between Summer Water Temperature and Summer Climate Indices

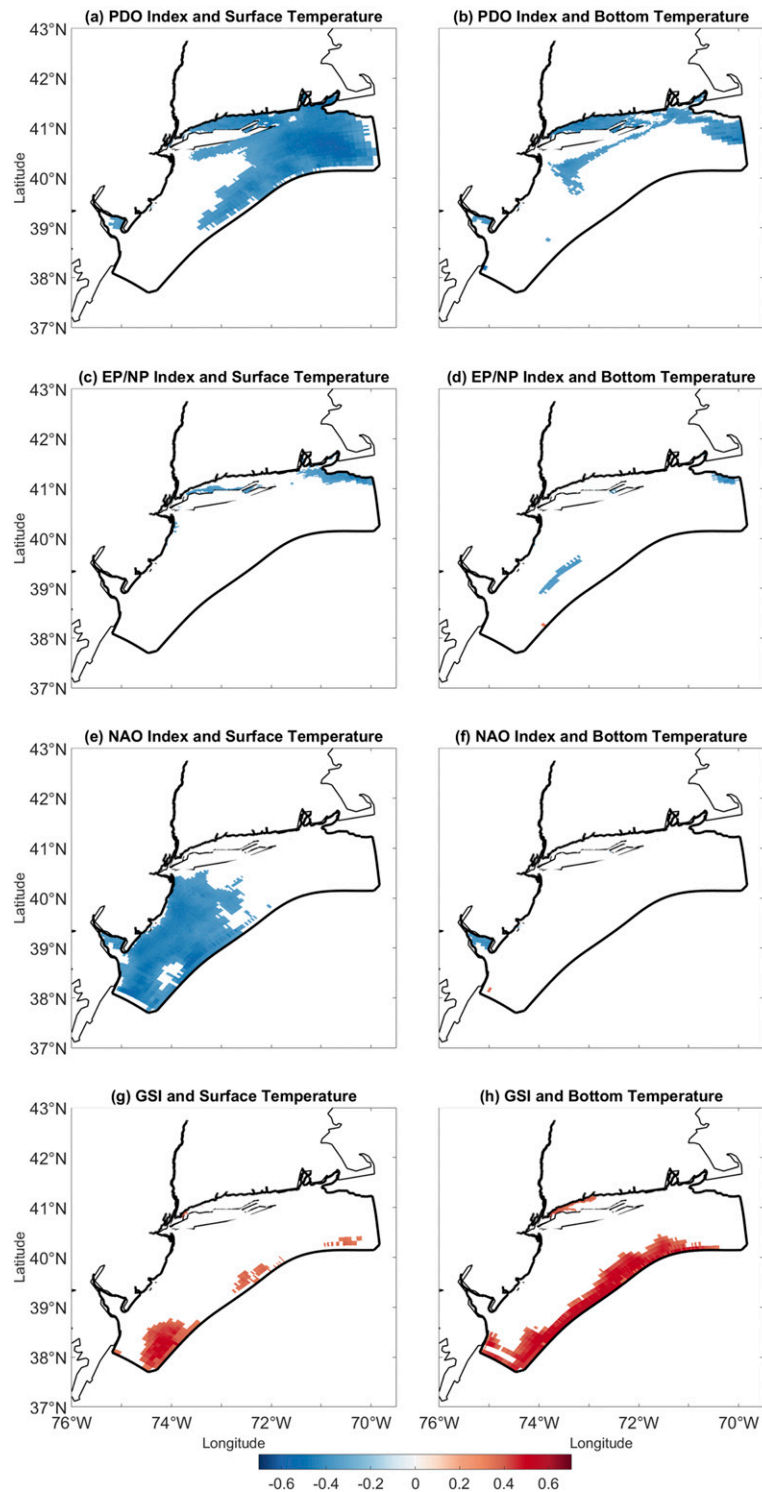


FIG. 9. Correlation between summer anomalies for the NYHOPS domain's surface and bottom water and summer indices for the (a),(b) PDO, (c),(d) EP/NP, (e),(f) NAO, and (g),(h) Gulf Stream position from 1979 to 2013. Only correlation coefficients statistically significant at the 5% level are displayed.

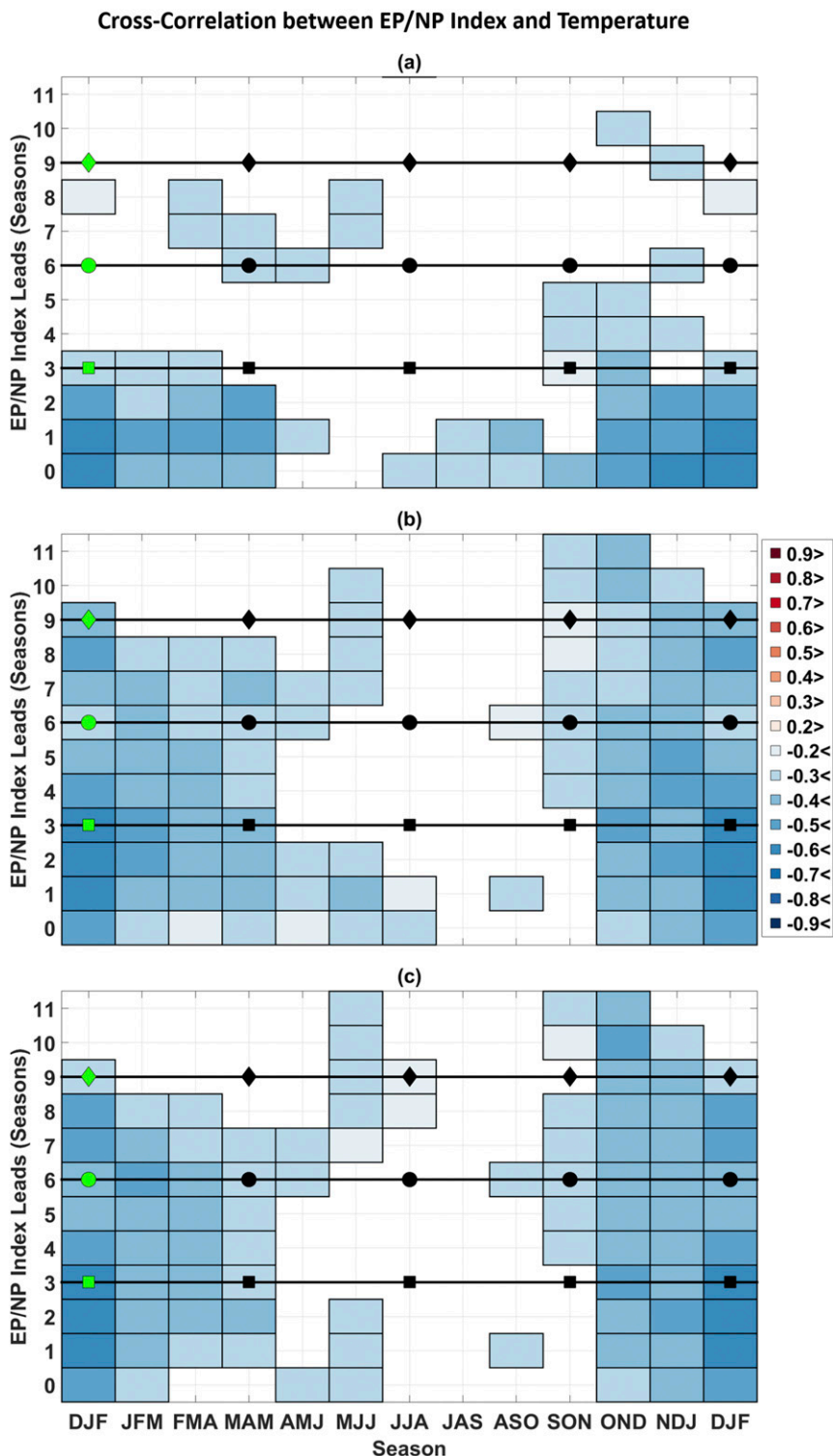


FIG. 10. Seasonal cross-correlation between the seasonally averaged EP/NP index and detrended seasonally averaged anomalies for (a) LIS air temperature, (b) LIS surface temperature, and (c) LIS bottom temperature from 1979 to 2013. Only correlation coefficients statistically significant at the 5% level are shown. Square, circular, and diamond-shaped markers represent the correlation between the season indicated on the horizontal axis and the first, second, and third nonoverlapping season, respectively. Colored markers indicate the relationships that are highlighted in the main text.

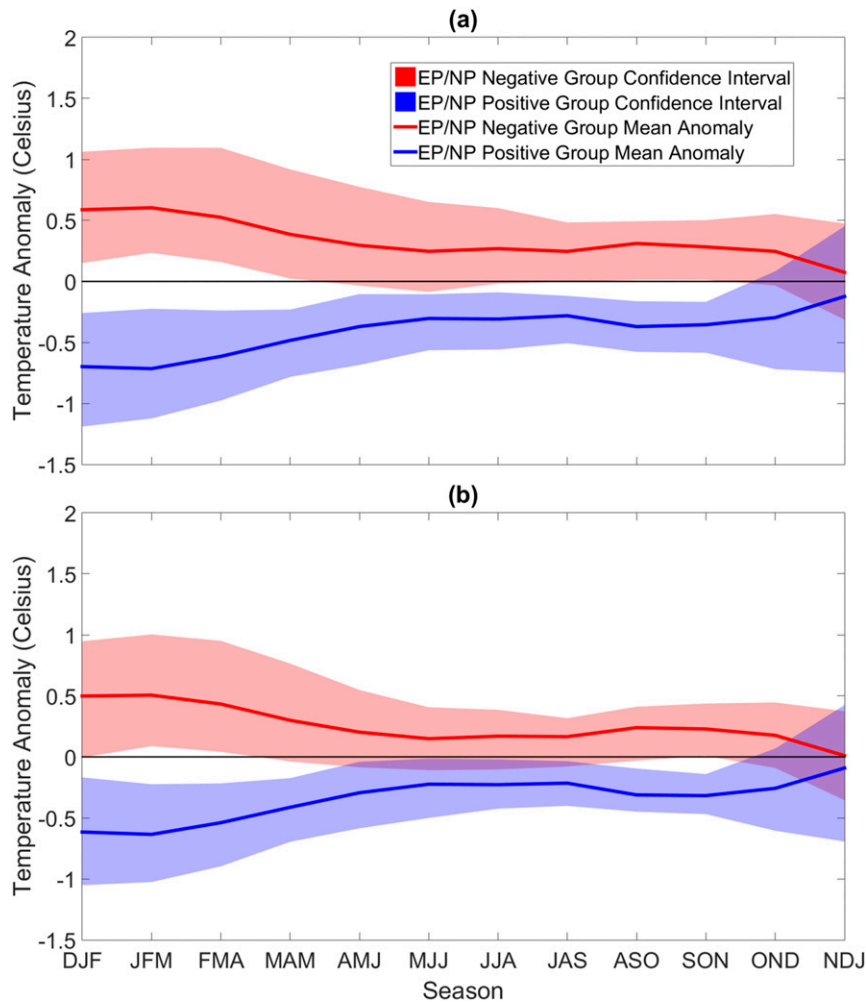


FIG. 11. (a) Composite means of nondetrended seasonally LIS surface water temperature anomalies for years when the DJF EP/NP index is positive (blue curve) and when the DJF EP/NP index is negative (red curve). Red and blue shaded regions are 95% confidence intervals associated with the composite means. (b) As in (a), but for detrended seasonally averaged LIS surface water temperature anomalies.

f. Composite analysis

To further test the robustness of the lagged relationships shown in Fig. 10, a composite analysis was performed. Composite means of seasonally averaged LIS water temperature anomalies were computed for years when the DJF EP/NP index was positive and for years when the DJF EP/NP index was negative. To determine if the two composite means were statistically different, a bootstrap resampling procedure (Efron 1979) was conducted in which 500 bootstrap replicates of the composite means were computed to estimate the sampling distributions corresponding to the composite means. 95% confidence intervals were then computed based on the estimated sampling distributions. Two means were

deemed statistically different at the 5% significance level if their corresponding 95% confidence intervals did not intersect.

As shown in Fig. 11, years for which the DJF EP/NP index is negative are associated with warmer-than-normal seasonally averaged LIS water temperature conditions from winter (DJF) through the summer (JJA). Similarly, years for which the DJF EP/NP index is positive are generally associated with negative seasonally averaged LIS water temperature anomalies from the winter through the summer. For the nondetrended analysis (Fig. 11a), the composite mean LIS water temperature anomalies associated with the positive and negative DJF EP/NP years are significantly different at the 5% level for all seasons except the

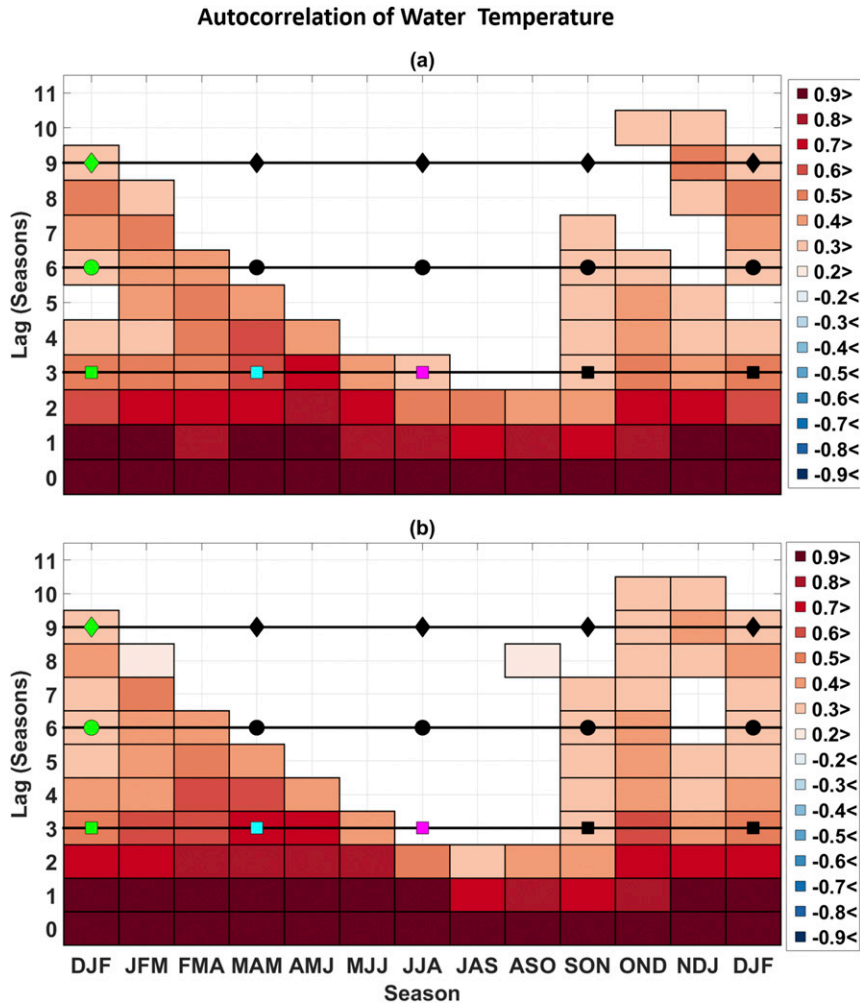


FIG. 12. Seasonal cycle of autocorrelation for seasonally averaged detrended LIS (a) surface and (b) bottom water temperature anomalies from 1979 to 2013. Only autocorrelation coefficients statistically significant at the 5% level are shown. Square, circular, and diamond-shaped markers represent the correlation between the season indicated on the horizontal axis and the first, second, and third nonoverlapping season, respectively. Colored markers indicate the relationships that are highlighted in the main text.

October–December (OND) and November–January (NDJ) seasons. The results for the detrended analysis (Fig. 11b) are similar except that the composite means are also not significantly different for the AMJ, May–July (MJJ), JJA, and July–September (JAS) seasons. The results from this composite analysis are consistent with the correlation analysis results presented in Fig. 10 because the results from both analyses suggest that years with negative (positive) DJF EP/NP indices are generally associated with positive (negative) subsequent seasonally averaged LIS water temperature anomalies. Both analyses thus support that idea that the DJF EP/NP pattern is an indicator of subsequent LIS water temperature conditions.

g. Seasonal persistence of water temperature

Further analyses explored explanations for cross-correlations of the EP/NP index with seasonally averaged LIS water temperature anomalies at numerous consecutive lags. A possible reason for the lagged relationships is that seasonally averaged LIS water temperature anomalies are autocorrelated. To test the autocorrelation hypothesis, we computed the seasonal cycle of autocorrelation of detrended seasonally averaged LIS water temperature anomalies.

Figure 12 shows that DJF water temperature anomalies are correlated with LIS water temperature anomalies in the subsequent canonical spring (green square)

and summer (green circle). However, the correlation between DJF LIS water temperature and summer LIS water temperature anomalies is rather weak, suggesting that not every DJF LIS water temperature anomaly will persist into the summer. MAM water temperature anomalies are shown to be strongly correlated with JJA water temperature anomalies (cyan squares). Figure 12 also suggests that seasonally averaged LIS water temperature anomalies in the winter, spring, and fall seasons are more autocorrelated than summer water temperature anomalies. For example, JJA bottom water temperature anomalies are not correlated with subsequent SON bottom water temperature anomalies, as indicated by the magenta square in Fig. 12. The results presented in Fig. 12 suggest that the reason why seasonally averaged EP/NP index is correlated with seasonally averaged water temperature anomalies at numerous consecutive lags is partially because of the autocorrelation of the water temperature anomalies.

Although Fig. 12 shows that seasonally averaged LIS water temperature anomalies are autocorrelated, it does not explain how the water temperature anomalies are generated. To show that LIS water temperature anomalies are strongly related to LIS air temperature anomalies, we computed the cross-correlation between seasonally averaged LIS air and water temperature anomalies. The results reveal that seasonally averaged air temperature anomalies can explain over 80% of LIS water temperature variability in the winter season and over 64% in the spring and fall seasons if one accounts for lags (Fig. 13). DJF and MAM LIS air temperature anomalies are both correlated with JJA bottom water temperature anomalies (green circle and cyan square, respectively) but only MAM air temperature anomalies are significantly correlated with JJA surface water temperature anomalies. JJA surface water temperature anomalies are more correlated with JJA air temperature anomalies than are JJA bottom water temperature anomalies, indicating that JJA surface water temperature anomalies more strongly reflect JJA air temperature conditions and that JJA bottom water temperature anomalies most strongly reflect air temperature conditions of prior seasons. Note that JJA LIS air temperature anomalies are not significantly correlated with SON LIS bottom or surface water temperature anomalies (magenta squares). This result can be interpreted physically as the summer shallow mixed layer containing the JJA LIS surface water temperature anomalies reflecting summer air temperature conditions being mixed with bottom water temperature anomalies by extratropical cyclones in the fall (Lentz et al. 2003). The results presented in Figs. 10 and 13 collectively suggest that the lagged relationship between the DJF EP/NP

index and water temperature is established through the influence of LIS air temperature on LIS water temperature.

The results shown in Fig. 13 also imply that an initially negative DJF water temperature anomaly can be reinforced in the spring if spring air temperature anomalies are negative. In such cases, a DJF water temperature anomaly is more likely to persist into the summer. The pronounced decadal variability of the EP/NP pattern (Fig. 4) and the EP/NP–air temperature relationships suggest that the anomalous atmospheric forcing that drives LIS water temperature variability has a tendency to reinforce the initial water temperature anomalies. In other words, the tendency for the EP/NP pattern to remain in a similar phase for a few years allows LIS water temperature anomalies to be reinforced or maintained by the EP/NP pattern until the EP/NP decadal mode changes sign. The reinforcement mechanism appears to have operated in 2011 and 2012 when a persistently negative EP/NP pattern helped maintained positive LIS air and water temperature anomalies for nearly a 2-yr period (Fig. 5). The EP/NP pattern is also seen to have been in a persistent negative phase during the 1991 and 1999 warm periods (Figs. 2 and 4). The enhanced EP/NP decadal variability may thus explain why LIS water temperature anomalies can persist for several seasons. The close relationship between air temperature and water temperature suggests that the degree of persistence will depend on the persistence of the atmospheric forcing.

A DJF water temperature anomaly can also be degraded if the subsequent spring air temperature anomaly is positive. In such cases, a DJF water temperature anomaly may not persist into the summer. Importantly, subsequent climatological spring air temperature conditions may not offset DJF water temperature anomalies if the DJF anomalies are initially very large. Thus, subsequent water temperature anomalies depend on the initial strength of the DJF water temperature anomalies as shown in Fig. 12 and on the subsequent air temperature conditions as shown in Fig. 13. This reasoning explains the existence of the lagged EP/NP index relationships with water temperature shown in Fig. 10 because stronger EP/NP phases are generally associated with larger air and water temperature anomalies that are less readily degraded by subsequent air temperature conditions.

h. Wavelet analysis

The cross-correlation analysis in section 4e detected the seasons for which the EP/NP pattern's influence on LIS water temperature is the strongest. However, the analysis provides little information about the time scales

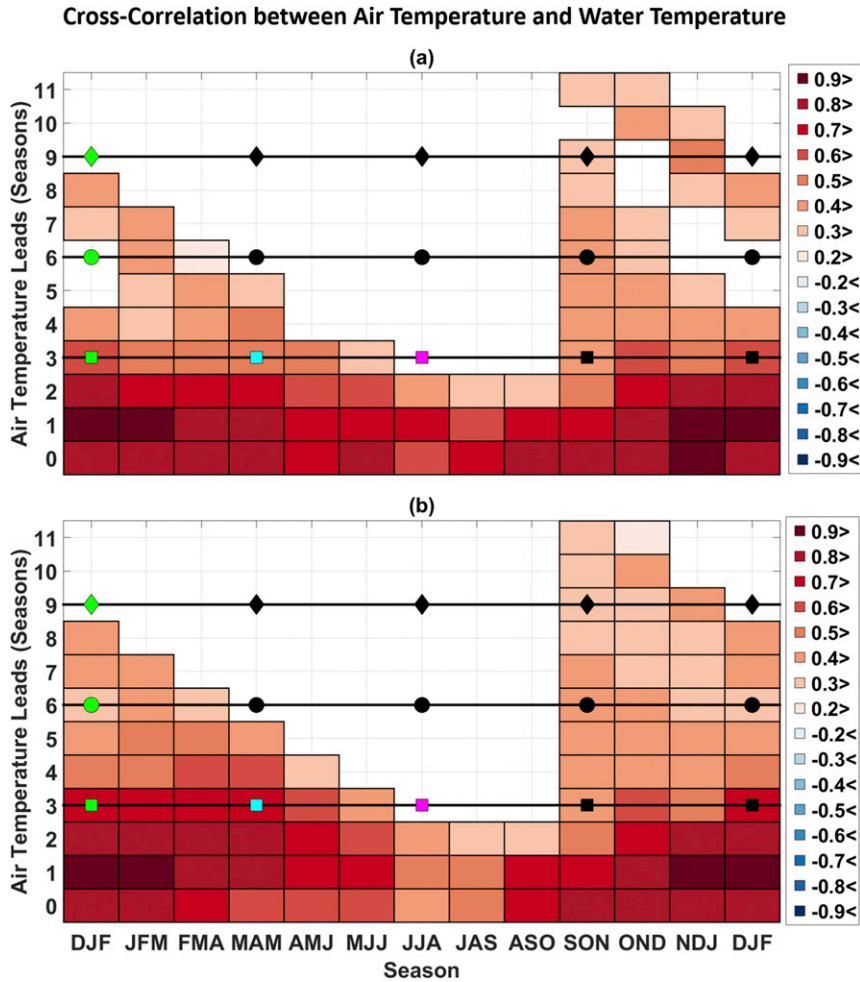


FIG. 13. Seasonal cycle of cross-correlation between seasonally average detrended LIS air temperature anomalies and detrended seasonally averaged anomalies for (a) LIS surface temperature and (b) LIS bottom temperature from 1979 to 2013. Only cross-correlation coefficients statistically significant at the 5% level are shown. Square, circular, and diamond-shaped markers represent the correlation between the season indicated on the horizontal axis and the first, second, and third nonoverlapping season, respectively. Colored markers indicate the relationships that are highlighted in the main text.

for which the EP/NP pattern’s influence is the strongest. As shown in Fig. 4, the EP/NP pattern is most energetic at decadal time scales so it is reasonable to hypothesize that anomalies for LIS air and water temperature vary coherently with the EP/NP index at decadal time scales given the strong correlation between the EP/NP index and LIS water temperature. Figures 14a and 15a provide qualitative evidence for coherent low-frequency fluctuations between the EP/NP pattern and anomalies for LIS air and water temperature. As shown in Figs. 14a and 1a, time periods when the EP/NP index is negative generally correspond to time periods when detrended LIS air and water temperature anomalies are positive. Conversely, time periods when the EP/NP index is

positive generally correspond to time periods when detrended LIS air and water temperature anomalies are negative.

To formally test the hypothesis that LIS air and water temperature anomalies fluctuated coherently with the EP/NP pattern at decadal time scales, the local wavelet squared coherence between the monthly EP/NP index and monthly detrended anomalies for LIS air and water temperature was computed. The wavelet coherence analysis results were found to be insensitive to the linear detrending of the data and therefore we only present the results from the detrended analysis.

Figures 14 and 15 show that statistically significant coherence is located at a period of 128 months, supporting

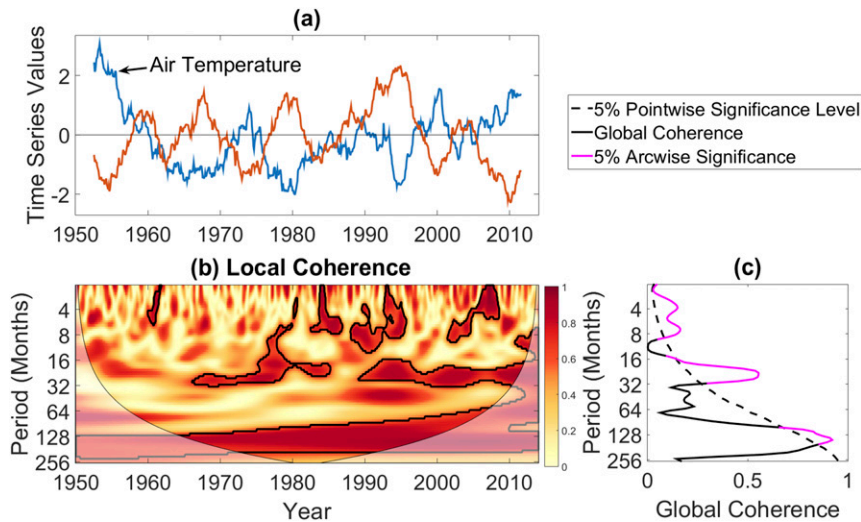


FIG. 14. (a) 5-yr running means of the monthly EP/NP index and detrended LIS air temperature time series. (b) Local wavelet coherence between detrended monthly LIS air temperature anomalies and the monthly EP/NP index. Contours enclose regions of 5% cumulative areawise significance and light shading represents the cone of influence. (c) The global wavelet coherence spectrum corresponding to (b).

the idea that monthly LIS air and water temperature anomalies fluctuate coherently with the EP/NP pattern on decadal time scales. Statistically significant coherence is also located at a period of 24 months. The similarity between EP/NP–air temperature and EP/NP–water temperature results is not surprising because LIS water temperature fluctuations are primarily governed by fluctuations in air temperature (Figs. 1b and 13). The statistically significant coherence at decadal time scales suggests that time periods when the decadal EP/NP mode shown in Fig. 4a is positive are

generally time periods when LIS air and water temperature anomalies are negative. Because wavelet coherence measures linear relationships, stronger EP/NP decadal fluctuations should produce stronger decadal fluctuations in LIS air and water temperature anomalies. Moreover, because the EP/NP pattern is correlated with 300-hPa streamfunction anomalies over the eastern United States (Fig. 7), time periods when the EP/NP decadal mode is positive are time periods when jet stream troughs are favored across the eastern United States. The strong coherence at a period of 128 months

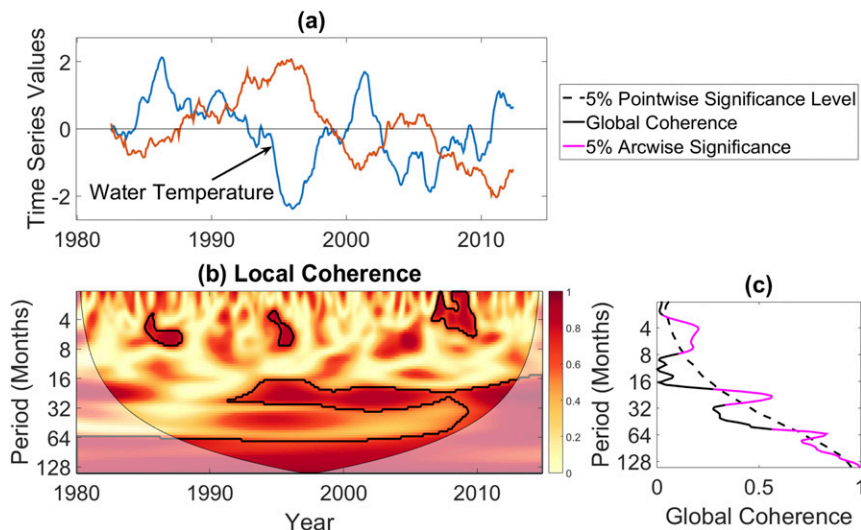


FIG. 15. As in Fig. 14, but for LIS surface water temperature anomalies.

therefore suggests that decadal fluctuations of LIS air and water temperature anomalies are the result of fluctuations in the eastern U.S. jet stream trough. As shown in Fig. 7, the EP/NP index is also correlated with 300-hPa streamfunction anomalies over Alaska, hence decadal LIS air and water temperature fluctuations are associated with changes in the so-called ridge–trough dipole that has received recent attention because of its role in driving U.S. temperature extremes (Wang et al. 2015). The high coherence of the EP/NP index with both LIS air and water temperature anomalies also suggests that temperature variability at those time scales is related fluctuations in the eastern U.S. trough rather than, say, perturbations in the Gulf Stream position that occur strongly on 7- to 10-yr time scales (Taylor 1995).

The wavelet analysis was also conducted between temperature and the GSI and between temperature and indices for the AMO and NAO. Surprisingly, the local and global coherence analysis produced no statistically significant results. A possible explanation for the lack of statistical significance is that the AMO is often associated with characteristic time scales greater than 20 years and so the record length used in this study may be too short to capture such low-frequency relationships.

i. Cumulative deviation analysis

Regime changes associated with the PDO and EP/NP indices are illustrated by conducting a cumulative deviation analysis of annual mean climate indices and nondetrended temperature anomalies. Computed annual means were standardized by their respective 1979–2013 standard deviations.

For both air (not shown) and surface water temperature (Fig. 16), there is a downward trend in the cumulative sums from 1979 to 1997, indicating the LIS water temperature anomalies are predominately negative during that period (Fig. 2). Similarly, for the PDO and EP/NP indices, there are upward trends in the cumulative sums from 1979 to 1997, though the cumulative sum for the EP/NP index is nearly zero from 1979 to 1990. At 1997, an inflection occurs and an upward trend in the cumulative sum for annual mean water temperature anomalies is present after 1997. The upward trend implies that annual mean water temperature anomalies are generally positive after 1997 (Fig. 2). Remarkably, around 1997 both the annual mean PDO and EP/NP indices appear to undergo a regime shift and downward trends in cumulative sums are present from 1997 to 2013, where the downward trends suggest that the 1997 to 2013 period is dominated by negative annual mean PDO and EP/NP indices. This result suggests that periods of warmer-than-normal conditions or colder-than-normal conditions are related to specific phases of the EP/NP

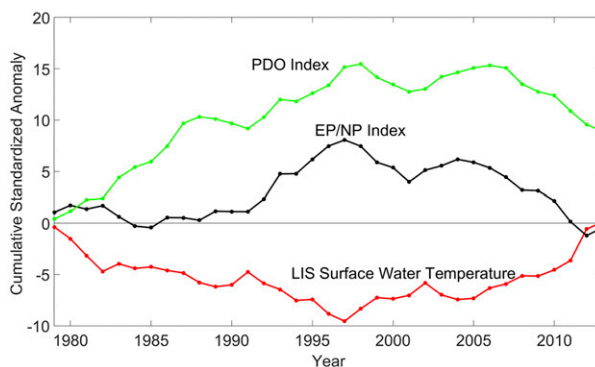


FIG. 16. Cumulative sum of standardized annual mean indices for the PDO and EP/NP and nondetrended standardized anomalies for LIS surface water temperature.

and PDO patterns, and hence the apparent warming trend of LIS water temperature since 1997 may be due to both natural climate variability and anthropogenic climate change.

5. Conclusions and discussion

Climate factors contributing to LIS water temperature variability were investigated. The PDO and EP/NP indices are strongly correlated with water temperature in the LIS. The PDO and EP/NP relationships with water temperature are stronger than the relationships of water temperature with the Gulf Stream position. The results suggest that LIS water temperature variability is primarily related to upstream atmospheric processes that render changes in the LIS thermal system.

Evidence was also found to support the idea that the EP/NP index may be skillful in making seasonal water temperature outlooks. The cross-correlation analysis (Fig. 10), in particular, shows that the DJF EP/NP index is a good predictor of subsequent MAM water temperature anomalies and also a predictor of JJA water temperature anomalies. This result suggests that the EP/NP index can be used to construct summer water temperature outlooks with lead times of 6 to 8 months. Such outlooks may prove useful for managing fisheries in the sense that stock assessments and harvest management of living marine resources can be informed by temperature projections based on previous EP/NP index values.

The EP/NP and PDO modes were found to be important to the historical variability of LIS water temperature and the results highlight how the influence of natural variability can be large. Importantly, the monthly EP/NP pattern has a characteristic time scale of 8 to 10 years (Fig. 4) and the detected characteristic time scale together with the wavelet coherence analysis results suggests that it may be possible to make assessments about LIS thermal

conditions from one decade to the next. As of the end of 2013, the quasi-decadal mode of the EP/NP index is positive (Fig. 3) and the wavelet analysis results indicate that it could progress to a negative phase given its 10-yr periodicity. Should the quasi decadal mode change phase, enhanced warming may be experienced across the LIS within the next five years because the negative EP/NP indices favor warmer-than-normal conditions that would be superimposed on the global warming signal. The rapid warming may negatively impact the already strained LIS that has experienced record warm temperature in recent years.

As diagnosed in this study, the PDO is composed of stochastic fluctuations, despite previous work showing strong variability at the annual time scale and in the 16–32-yr period band (Chan and Zhou 2005; Lara et al. 2016). The stochastic nature of PDO will pose a challenge in determining when it will change prominent sign and thus also in assessing its future impact on the LIS thermal system.

Recent work by Chen et al. (2014, 2015) showed that the anomalously warm mid-Atlantic water temperatures across the mid-Atlantic Bight during the first half of 2012 were related mainly to air-sea heat fluxes. The regime changes shown in Fig. 16 suggest that the water temperature anomalies may have been related to the preferential expression of negative EP/NP phases that set up atmospheric patterns conducive to generating anomalously warm water temperatures. Consistently, for January and February of 2012, the EP/NP index was strongly negative, the January index equal to -1.92 and the February index equal to -0.33 (Fig. 5). For January, the index corresponds to the second strongest negative January EP/NP index since 1950 behind the January 1964 index of -1.95 . According to the correlation analysis results shown in Fig. 7 and Table 1, the negative EP/NP phases should have contributed to warmer-than-normal LIS water temperatures in the of spring 2012 in agreement with Chen et al. (2015), who showed that the spring water temperature anomalies were related to winter atmospheric circulation anomalies. The record negative March 2012 EP/NP index of -2.59 (Fig. 5) suggests that atmospheric forcing enhanced the preexisting anomalies. The cumulative anomaly analysis supports the conclusion that the March 2012 event may have been related to a North Pacific regime shift that enhanced the probability of occurrence of atmospheric conditions favoring mid-Atlantic Bight warming.

As shown by Pershing et al. (2015), the PDO index is a good predictor ($r = -0.67$) of summer water temperature across the Gulf of Maine. The result is similar to that found in the present study, where the PDO is also a good predictor of summer LIS water temperature. The

similarity between the results is consistent with how LIS water temperature is strongly correlated with air temperature across the U.S. Northeast (Fig. 1b) and water temperature across the Gulf of Maine (Fig. 6). The correlation between LIS water temperature and water temperature across a large coastal region is not surprising given the large spatial scale of the EP/NP pattern (Fig. 7c) and the dominant influence of the EP/NP pattern on U.S. Northeast temperature variability (Schulte and Lee 2017). The correlation between LIS water temperature and water temperature around the Gulf of Maine could mean that the wintertime EP/NP pattern could also influence Gulf of Maine water temperature. Given that the PDO and EP/NP indices are highly correlated, the summer water temperature–PDO relationship identified by Pershing et al. (2015) could actually reflect the EP/NP influences on U.S. temperature and the underlying North Pacific SSTs. Indeed, studies suggest that the atmosphere drives the PDO variability rather than the PDO drives the atmospheric variability. Future work is needed to better understand the precise mechanism that relates the PDO to LIS and Gulf of Maine water temperature variability.

The results from this study may have important implications for understanding how biological communities in the LIS may respond to large-scale climate patterns. As noted by previous studies, the PDO shifted prominent sign in 1976, 1989, and 1997, marking North Pacific climatic regime shifts (Hare and Mantua 2000; Hong et al. 2014). Multivariate analyses of LIS finfish abundance indices identified a shift in spring community structure as it related to water temperature (Howell and Auster 2012) and produced two primary year groupings: 1984–98 (cold period) and 1999–2008 (warm period). Two years after the 1997 regime shift, the LIS American lobster population dramatically declined (Pearce and Balcom 2005) and has not fully recovered despite efforts to manage the harvest. Collie et al. (2008) found biological communities across the Rhode Island Sound to be related to spring–summer water temperature. The results from this study therefore suggest that the biological communities could also be related to the EP/NP pattern because of the EP/NP pattern's strong influence on water temperature around the LIS region. These studies suggests that biological communities may be impacted by the PDO and EP/NP because these patterns are related to LIS temperature variability, as diagnosed in the present study.

The low-frequency relationships between water temperature and the EP/NP pattern pose a challenge in extrapolating anthropogenic-related LIS water temperature trends. The generally positive PDO index in the first half of the 34-yr hindcast period would have contributed to LIS cooling according to the correlation

analysis, whereas the predominately negative PDO index in the latter half would have favored LIS warming. The result is a contribution to overall positive trend in the LIS temperature record. This modulation mechanism is supported by the mechanism identified by Trenberth et al. (2014), who showed that an upper-tropospheric teleconnection pattern resembling that associated with the PDO is capable of increasing the odds of regional climate anomalies. It is therefore simplistic to say that the 1979 to 2013 trend in LIS water temperature is solely due to anthropogenic causes. It is also important to note that the EP/NP pattern may itself be influenced by anthropogenic forcing through increases in SSTs, enhancements of tropical convection across the western Pacific, and the strengthening of the Alaskan ridge (Wang et al. 2014). Further research is needed to reliably estimate the anthropogenic impacts on LIS temperature changes. For example, the capability of global climate models to reproduce the historical EP/NP pattern could be assessed and then, if the historical pattern is well reproduced, additional experiments could be conducted under various greenhouse gas emission scenarios to diagnose a relationship between greenhouse gas emissions and the behavior of the EP/NP pattern.

The results presented in this study provide compelling evidence that LIS water temperature variability is influenced by North Pacific variability more than by North Atlantic variability. The results suggest that future work should focus on understanding North Pacific phenomena, particularly the response of North Pacific atmospheric phenomena to climate change, as such information could prove most useful in understanding the future of the LIS ecosystem and the future ecosystems of other temperate estuaries in the U.S. Northeast such as the Delaware and Chesapeake Bays.

Acknowledgments. Financial support was provided by the Long Island Sound Study and the NY and CT Sea Grants through the project R/CE-33-NYCT.

APPENDIX

Cumulative Arcwise Testing

The computation of a global wavelet quantity results in a function $g(s)$ describing how the wavelet quantity changes with wavelet scale. The graph of $g(s)$ is the set

$$S = \{[s, g(s)]\}. \quad (\text{A1})$$

The application of the pointwise test at the α_i level results in the subset of the graph

$$S_i = \{[s, g(s)]: g(s) > F_i(s)\}, \quad (\text{A2})$$

where $F_i(s)$ is the critical level of the pointwise test associated with the significance level α_i . A significant arc a_i corresponding to α_i is a contiguous (no gaps) subset of S_i such that there is no larger contiguous subset containing it. Intuitively, arcs are isolated pieces of the graph S with no gaps or breaks.

The application of the pointwise significance test at N pointwise significance levels $\alpha_1, \alpha_2, \dots, \alpha_N$ results in the nested sequence of arcs (referred to as a geometric pathway, hereafter)

$$a_1 \subset a_2 \subset \dots \subset a_N, \quad (\text{A3})$$

where the geometric pathway has length N and a_N is the last element of the geometric pathway. Because global peaks widen with increasing wavelet scale as a result of the underlying reproducing kernel (Maraun and Kurths 2004) it is important to compute the logarithm (base 2) of the wavelet scales before computing the arc length. Furthermore, one can normalize the computation of arc length by dividing $g(s)$ by $F_1(s)$. Thus, S_i in the normalized coordinate system is given by

$$S_i = \left\{ \left[\log_2 s, g(s)/F_1(s) \right] : g(s) > F_i(s) \right\}. \quad (\text{A4})$$

This normalization allows one to readily compare peaks at different scales and between global spectra associated with different time series. Associate to each a_j the quantity γ_j defined as the cumulative normalized arc length of the last $N - j + 1$ elements of a geometric pathway with length N . The output of the arcwise testing procedure is the largest member of the geometric pathway such that its test statistic exceeds the critical level of the test γ_{crit} . The largest member is the one with the greatest arc length. The critical level of test is calculated in a similar manner to the two-dimensional case but area is replaced by arc length. The arcwise test was applied at the 5% significance level using pointwise significance levels ranging from 0.02 to 0.12, the spacing between adjacent significance levels equal to 0.02.

REFERENCES

- Barnston, A. G., and R. E. Livezey, 1987: Classification, seasonality and persistence of low-frequency atmospheric circulation patterns. *Mon. Wea. Rev.*, **115**, 1083–1126, [https://doi.org/10.1175/1520-0493\(1987\)115<1083:CSAPOL>2.0.CO;2](https://doi.org/10.1175/1520-0493(1987)115<1083:CSAPOL>2.0.CO;2).
- Chan, J. C. L., and W. Zhou, 2005: PDO, ENSO and the early summer monsoon rainfall over south China. *Geophys. Res. Lett.*, **32**, L08810, <https://doi.org/10.1029/2004GL022015>.

- Chen, K., G. G. Gawarkiewicz, S. J. Lentz, and J. M. Bane, 2014: Diagnosing the warming of the northeastern U.S. coastal ocean in 2012: A linkage between the atmospheric jet stream variability and ocean response. *J. Geophys. Res. Oceans*, **119**, 218–227, <https://doi.org/10.1002/2013JC009393>.
- , —, Y.-O. Kwon, and W. G. Zhang, 2015: The role of atmospheric forcing versus ocean advection during the extreme warming of the northeast U.S. continental shelf in 2012. *J. Geophys. Res. Oceans*, **120**, 4324–4339, <https://doi.org/10.1002/2014JC010547>.
- Cloern, J. E., and Coauthors, 2010: Biological communities in San Francisco Bay track large-scale climate forcing over the North Pacific. *Geophys. Res. Lett.*, **37**, L21602, <https://doi.org/10.1029/2010GL044774>.
- Collie, J. S., A. D. Wood, and H. P. Jeffries, 2008: Long-term shifts in the species composition of a coastal fish community. *Can. J. Fish. Aquat. Sci.*, **65**, 1352–1365, <https://doi.org/10.1139/F08-048>.
- Di Lorenzo, E., and Coauthors, 2008: North Pacific Gyre Oscillation links ocean climate and ecosystem change. *Geophys. Res. Lett.*, **35**, L08607, <https://doi.org/10.1029/2007GL032838>.
- Efron, B., 1979: Bootstrap methods: Another look at the jackknife. *Ann. Stat.*, **7**, 1–26, <https://doi.org/10.1214/aos/1176344552>.
- Elsayed, M. A. K., 2006: A novel technique in analyzing non-linear wave–wave interaction. *Ocean Eng.*, **33**, 168–180, <https://doi.org/10.1016/j.oceaneng.2005.04.010>.
- Georgas, N., and Coauthors, 2016: An open-access, multi-decadal, three-dimensional, hydrodynamic hindcast dataset for the Long Island Sound and New York/New Jersey harbor estuaries. *J. Mar. Sci. Eng.*, **4**, 48, <https://doi.org/10.3390/jmse4030048>.
- Grinsted, A., J. C. Moore, and S. Jevrejeva, 2004: Application of the cross wavelet transform and wavelet coherence to geophysical time series. *Nonlinear Processes Geophys.*, **11**, 561–566, <https://doi.org/10.5194/npg-11-561-2004>.
- Guttman, N. B., and R. G. Quayle, 1996: A historical perspective of U.S. climate divisions. *Bull. Amer. Meteor. Soc.*, **77**, 293–303, [https://doi.org/10.1175/1520-0477\(1996\)077<0293:AHPOUC>2.0.CO;2](https://doi.org/10.1175/1520-0477(1996)077<0293:AHPOUC>2.0.CO;2).
- Hare, S. R., and N. J. Mantua, 2000: Empirical evidence for North Pacific regime shifts in 1977 and 1989. *Prog. Oceanogr.*, **47**, 103–145, [https://doi.org/10.1016/S0079-6611\(00\)00033-1](https://doi.org/10.1016/S0079-6611(00)00033-1).
- Hartmann, D. L., 2015: Pacific sea surface temperature and the winter of 2014. *Geophys. Res. Lett.*, **42**, 1894–1902, <https://doi.org/10.1002/2015GL063083>.
- Hong, C.-C., Y.-K. Wu, T. Li, and C.-C. Chang, 2014: The climate regime shift over the Pacific during 1996/1997. *Climate Dyn.*, **43**, 435–446, <https://doi.org/10.1007/s00382-013-1867-9>.
- Howell, P., and P. J. Auster, 2012: Phase shift in an estuarine finfish community associated with warming temperatures. *Mar. Coastal Fish.*, **4**, 481–495, <https://doi.org/10.1080/19425120.2012.685144>.
- Hurrell, J. W., 1995: Decadal trends in the North Atlantic Oscillation: Regional temperatures and precipitation. *Science*, **269**, 676–679, <https://doi.org/10.1126/science.269.5224.676>.
- Kerr, R. A., 2000: A North Atlantic climate pacemaker for the centuries. *Science*, **288**, 1984–1985, <https://doi.org/10.1126/science.288.5473.1984>.
- Lara, C., G. S. Saldías, F. J. Tapia, J. L. Iriarte, and B. R. Broitman, 2016: Interannual variability in temporal patterns of Chlorophyll-a and their potential influence on the supply of mussel larvae to inner waters in northern Patagonia (41–44°S). *J. Mar. Syst.*, **155**, 11–18, <https://doi.org/10.1016/j.jmarsys.2015.10.010>.
- Lentz, S., K. Shearman, S. Anderson, A. Plueddemann, and J. Edson, 2003: Evolution of stratification over the New England shelf during the Coastal Mixing and Optics study, August 1996–June 1997. *J. Geophys. Res.*, **108**, 3008, <https://doi.org/10.1029/2001JC001121>.
- Mantua, N. J., S. R. Hare, Y. Zhang, J. M. Wallace, and R. C. Francis, 1997: A Pacific interdecadal climate oscillation with impacts on salmon production. *Bull. Amer. Meteor. Soc.*, **78**, 1069–1079, [https://doi.org/10.1175/1520-0477\(1997\)078<1069:APICOW>2.0.CO;2](https://doi.org/10.1175/1520-0477(1997)078<1069:APICOW>2.0.CO;2).
- Maraun, D., and J. Kurths, 2004: Cross wavelet analysis: Significance testing and pitfalls. *Nonlinear Processes Geophys.*, **11**, 505–514, <https://doi.org/10.5194/npg-11-505-2004>.
- , —, and M. Holschneider, 2007: Nonstationary Gaussian processes in wavelet domain: Synthesis, estimation, and significance testing. *Phys. Rev. E*, **75**, 016707, <https://doi.org/10.1103/PhysRevE.75.016707>.
- Newman, M., and Coauthors, 2016: The Pacific decadal oscillation, revisited. *J. Climate*, **29**, 4399–4427, <https://doi.org/10.1175/JCLI-D-15-0508.1>.
- Palmer, T. N., 2014: Record-breaking winters and global climate change. *Science*, **344**, 803–804, <https://doi.org/10.1126/science.1255147>.
- , and D. A. Mansfield, 1984: Response of two atmospheric general circulation models to sea surface temperature anomalies in the tropical east and west Pacific. *Nature*, **310**, 483–485, <https://doi.org/10.1038/310483a0>.
- Pearce, J., and N. Balcom, 2005: The 1999 Long Island Sound lobster mortality event: Findings of the comprehensive research initiative. *J. Shellfish Res.*, **24**, 691–697, [https://doi.org/10.2983/0730-8000\(2005\)24\[691:TLISLM\]2.0.CO;2](https://doi.org/10.2983/0730-8000(2005)24[691:TLISLM]2.0.CO;2).
- Pershing, A. J., and Coauthors, 2015: Slow adaptation in the face of rapid warming leads to collapse of the Gulf of Maine cod fishery. *Science*, **350**, 809–812, <https://doi.org/10.1126/science.aac9819>.
- Schulte, J. A., 2016: Cumulative areawise testing in wavelet analysis and its application to geophysical time series. *Nonlinear Processes Geophys.*, **23**, 45–57, <https://doi.org/10.5194/npg-23-45-2016>.
- , and S. Lee, 2017: Strengthening North Pacific influences on United States temperature variability. *Sci. Rep.*, **7**, 124, <https://doi.org/10.1038/s41598-017-00175-y>.
- , C. Duffy, and R. G. Najjar, 2015: Geometric and topological approaches to significance testing in wavelet analysis. *Nonlinear Processes Geophys.*, **22**, 139–156, <https://doi.org/10.5194/npg-22-139-2015>.
- , R. G. Najjar, and M. Li, 2016: The influence of climate modes on streamflow in the mid-Atlantic region of the United States. *J. Hydrol. Reg. Stud.*, **5**, 80–99, <https://doi.org/10.1016/j.ejrh.2015.11.003>.
- Simmons, A. J., J. M. Wallace, and G. W. Branstator, 1983: Barotropic wave propagation and instability, and atmospheric teleconnection patterns. *J. Atmos. Sci.*, **40**, 1363–1392, [https://doi.org/10.1175/1520-0469\(1983\)040<1363:BWPATA>2.0.CO;2](https://doi.org/10.1175/1520-0469(1983)040<1363:BWPATA>2.0.CO;2).
- Taylor, A. H., 1995: North–south shifts of the Gulf Stream and their climatic connection with the abundance of zooplankton in the UK and its surrounding seas. *ICES J. Mar. Sci.*, **52**, 711–721, [https://doi.org/10.1016/1054-3139\(95\)80084-0](https://doi.org/10.1016/1054-3139(95)80084-0).
- Thompson, D. W. J., and J. M. Wallace, 1998: The Arctic Oscillation signature in the wintertime geopotential height and

- temperature fields. *Geophys. Res. Lett.*, **25**, 1297–1300, <https://doi.org/10.1029/98GL00950>.
- Torrence, C., and G. P. Compo, 1998: A practical guide to wavelet analysis. *Bull. Amer. Meteor. Soc.*, **79**, 61–78, [https://doi.org/10.1175/1520-0477\(1998\)079<0061:APGTWA>2.0.CO;2](https://doi.org/10.1175/1520-0477(1998)079<0061:APGTWA>2.0.CO;2).
- Trenberth, K. E., J. T. Fasullo, G. Branstator, and A. S. Phillips, 2014: Seasonal aspects of the recent pause in surface warming. *Nat. Climate Change*, **4**, 911–916, <https://doi.org/10.1038/nclimate2341>.
- Wallace, J. M., and D. S. Gutzler, 1981: Teleconnections in the geopotential height field during the Northern Hemisphere winter. *Mon. Wea. Rev.*, **109**, 784–812, [https://doi.org/10.1175/1520-0493\(1981\)109<0784:TITGHF>2.0.CO;2](https://doi.org/10.1175/1520-0493(1981)109<0784:TITGHF>2.0.CO;2).
- Wang, S.-Y., L. Hipps, R. R. Gillies, and J.-H. Yoon, 2014: Probable causes of the abnormal ridge accompanying the 2013–2014 California drought: ENSO precursor and anthropogenic warming footprint. *Geophys. Res. Lett.*, **41**, 3220–3226, <https://doi.org/10.1002/2014GL059748>.
- , W.-R. Huang, and J.-H. Yoon, 2015: The North American winter “dipole” and extremes activity: A CMIP5 assessment. *Atmos. Sci. Lett.*, **16**, 338–345, <https://doi.org/10.1002/asl2.565>.